PROCESS OPTIMIZATION OF 3D PRINTING WITH CONTINUOUS FIBER REINFORCED UV CURABLE THERMOSET RESIN

A Thesis
Submitted to the Graduate Faculty
of the
North Dakota State University
of Agriculture and Applied Science

By
Md Atikur Rahman

In Partial Fulfillment of the Requirements
for the Degree of
MASTER OF SCIENCE

Major Department:
Mechanical Engineering

July 2022

Fargo, North Dakota

North Dakota State University
Graduate School

Title

PROCESS OPTIMIZATION OF 3D PRINTING WITH CONTINUOUS FIBER REINFORCED UV CURABLE THERMOSET RESIN

By

Md Atikur Rahman

The Supervisory Committee certifies that this ***disquisition*** complies with North Dakota State University's regulations and meets the accepted standards for the degree of

MASTER OF SCIENCE

SUPERVISORY COMMITTEE:

Dr. Chad Ulven
Chair

Dr. Majura Selekwa

Dr. Dean Webster

Approved:

November 9, 2022
Date

Dr. Chad Ulven
Department Chair

ABSTRACT

3D printed polymer components cannot be used as structural components due to the 3D printable material property limitations. To improve mechanical properties, a composite 3D printer is developed and studied. Technical aspects of 3D printing with continuous carbon fiber reinforced dual UV and thermal curable thermoset composite were experimented. To optimize the 3D printing process parameters, the effect of printing nozzle size, line spacing of the print, and resin flow rate was studied. To achieve minimum void content and maximum fiber volume fraction, print parameter configurations were studied using microscopic surface roughness analysis. The tensile and flexural properties of 3D printed specimens were tested. Results of the study indicated that impressive mechanical properties of the 3D printed continuous fiber reinforced UV curable thermoset composite can be achieved through the optimization of printing parameters.

ACKNOWLEDGMENTS

The author would like to extend special acknowledgements to Army Research Lab and North Dakota State University for funding and facilitating this study. Dr. Chad A. Ulven's contribution of supervising this study deserves special acknowledgement. The author would like to thank Luke Gibbon, Riley Helena, Zach Kuhn, Jena Marcolina and Jakob Sailor for their relentless help.

DEDICATION

Dedicated to Syed Zia Uddin & Feroj Al Moshrakin. These friends guided me, helped me through tough times.

TABLE OF CONTENTS

LIST OF TABLES

LIST OF FIGURES

LIST OF ABBREVIATIONS

ANOVA .....Analysis of Variance

AM .....Additive Manufacturing

CAD .....Computer Aided Design

CF.....Carbon Fiber

DLP .....Digital Light Processing

DMA .....Dynamic Mechanical Analysis

FDM.....Fused Deposition Modelling

FRC.....Fiber Reinforced Composite

LED.....Light Emitting Diode

ROM .....Rule of Mixture

SLA.....Stereolithography

TGA .....Thermogravimetric Analysis

UV.....Ultraviolet

LIST OF SYMBOLS

A .....Cross sectional area

b .....Width of specimen

D .....Maximum flexural deflection

d .....Depth of specimen

d_F .....Fiber prepreg diameter

d_N .....Nozzle diameter

E .....Tensile elastic modulus

E_c.....Tensile elastic modulus of composite

E_f.....Tensile elastic modulus of fiber

E_m .....Tensile elastic modulus of matrix

E_{fl} .....Flexural elastic modulus

L .....Length of specimen

P .....Applied force

s .....Print speed

S_a.....Average surface roughness

T_g.....Glass transition temperature

V_f .....Fiber volume fraction

V_{fp} .....Fiber volume fraction of prepreg

V_m .....Matrix volume fraction

V_{pr} .....Void fraction originating from process flaw

V_s .....Void fraction originating from shrinkage

V_{ti} .....Void fraction originating from thermal initiator evaporation

V_v .....Void volume fraction

$\dot{V}_r$ .....Resin flow rate

w_f .....mass of fiber tow

w_m .....mass of matrix

w_p .....mass of prepreg

ε_{cu} .....Ultimate tensile strain of composite

ε_{fl} .....Flexural strain

ε_{fu} .....Ultimate tensile strain of fiber

ε_{mu} .....Ultimate tensile strain of matrix

ε_t .....Tensile strain

ρ_f .....Density of fiber filament

ρ_r .....Density of resin

σ_{cu} .....Ultimate tensile stress of composite

σ_{fl} .....Flexural stress

σ_{fu} .....Ultimate tensile stress of fiber

σ_{mu} .....Ultimate tensile stress of matrix

σ_t .....Tensile stress

LIST OF APPENDIX TABLES

1. INTRODUCTION

Additive manufacturing (AM), also known as 3D printing, offers much flexibility over conventional manufacturing processes. Traditional manufacturing techniques require a high volume of units to be produced for the product to be cost-effective. Thus, custom design products are expensive when manufactured with traditional techniques. On the other hand, AM adds material to the part in a layer-by-layer fashion according to the computer aided design (CAD). This manufacturing style offers an automated method of producing custom parts at a meager cost [1]. Moreover, 3D printing technologies can manufacture parts with intricate design and complex geometry [2]. These capabilities of the AM process have placed itself in a high-demand position in numerous industries [3, 4].

Most 3D printing methods were first patented and commercialized during the 1980s and 1990s [5]. The first form of 3D printing was patented in the form of Stereolithography (SLA) in 1986 [6]. SLA technology uses UV light exposure on a photocurable thermosetting resin [7]. Another variant of 3D printing with photocurable thermosetting resin is digital light processing (DLP) [8]. In 1989 Stratasys introduced fused deposition modelling, which melts thermoplastic in a heated extrusion nozzle and lays the molten material according to the designed paths [9]. These 3D printing technologies, utilizing polymer materials, are vastly flexible and adaptive in design geometries [10]. However, the 3D printed products display poor mechanical properties (i.e., strength, elastic moduli, and toughness) [11]. Two significant sources of these shortcomings are poor interlaminar adhesion and a limited number of 3D printable materials [12]. The first 3D printed products were used for prototyping, design verification, and proof of idea. For these limited purposes, initially, the inferior mechanical properties of the 3D printed parts were acceptable. Nevertheless, 3D printing has made its way into thousands of applications from consumer

products, biomechanics, prosthetics, aerospace applications, and many more [13-15]. The potential of this powerful technology is now held back, mainly due to the material properties. As a result, the demand for material enhancement research for 3D printing has increased significantly.

One of the most significant advancements in material science in modern times is the advancement of composite materials. The composite approach of materials has facilitated the production of lightweight and high-performing components in many applications. Aerospace, automobile, prosthetics, and wind turbines are some sectors that have observed massive incorporation of composite materials. Moreover, the mechanical properties of composite materials can be tailored within wide ranges. The fiber orientation of the composite materials dictates the anisotropic mechanical properties of the composite. By altering the fashion of fiber distribution in the composite, the overall mechanical properties of the composite can be altered in different direction relative to the fiber layup directions. For this reason, the tunability of mechanical properties of composite materials is highly directional. The composite materials' improved performance, lightweight, tunability, and directional anisotropy are all desirable traits for 3D printed components. Due to the combination of these potentials, along with its challenges, 3D printing with composite materials is a sought-after technology in AM research [16, 17].

Depending on the size of reinforcement, composite materials can be broadly categorized into three major types- particle reinforced, short fiber reinforced, and continuous fiber-reinforced composites. These all have their pros and cons. Short-fiber reinforced composites (FRC) are low-cost to manufacture. The processing, manufacturing, and printing with these composites are straightforward. On the other hand, continuous fiber composites are difficult and expensive to manufacture. However, continuous fiber-reinforced composite materials offer the highest mechanical properties and most control over the directional distribution of these properties

compared to other composites [18]. In this research, 3D printing technology with photocurable thermosetting resin is the topic of focus. This research is specifically aimed at developing a 3D printing technology utilizing a UV curable thermosetting resin system reinforced with continuous fiber reinforcement.

1.1. 3D Printing with UV Curable Resin

Stereolithography (SLA) and digital light processing (DLP) printers use UV curable resin systems for 3D printing. In SLA and DLP 3D printing, UV light is projected on a flat surface of UV curable resin. Projection of the UV light on the liquid resin initiates a polymerization reaction and solidifies the resin at the projection spot. In this method, a thin layer is cured, and then another layer of liquid resin is deposited on the previous layer. This process is repeated to build multiple layers. Both SLA and DLP have two orientations of build platform movement, “top-down” and “bottom-up” orientations. The build plate moves downwards in the top-down approach, and liquid resin is deposited on top of the previous layers. In this approach, UV light is projected directly on the resin. UV light is projected through a transparent hydrophobic surface in the bottom-up approach. The liquid resin between the previous layers and the hydrophobic surface is cured when UV light is cast on it [19]. The cured layer sticks to the previous layer or base plate, but it does not adhere to the hydrophobic transparent surface due to its low surface energy property [19].

Principal components of the UV curable resin systems are oligomers, diluents (monomers), and photoinitiators. Standard resin systems for these printing technologies are acrylate oligomers. However, the literature has reported experiments with acrylate epoxy, acrylate urethanes, acrylate polyesters, polyether, and silicones as oligomers. Shukla et al.[20] provided a thorough review study on the UV curable resin chemistry. Acrylates are heavily used in UV-cured 3D printing because of their high reactivity and fast reaction time of a fraction of a second. Exposure to UV

light in the resin energizes the photoinitiators, generating free radicals [21]. These free radicals initiate the polymerizations reaction between oligomers and monomers [22, 23]. The depth of the reaction zones depends on the resin type and the laser power and focus. After the printing, a tiny portion of liquid resin is left uncured in the printed body. To fully cure, the part is post-cured with further prolonged UV exposure [24].

Table 1 [25] shows comparative mechanical properties of currently commercially available UV curable SLA resin systems from different manufacturers. The commercial manufacturer of the resins usually provides these properties. These properties of the final product can still vary depending upon several process parameters, i.e., UV spot focus diameter, UV light intensity, exposure time, layer thickness, temperature, inclusion or modification of resin system, and post-processing parameters. Although the properties are variable, the final printed parts are largely brittle and have lower mechanical strength than traditional injection molded parts.

Table 1: Properties of SLA resins [25]

	Standard & Clear	**Tough**	**Durable**	**Heat Resistant**	**Ceramic Reinforced**
Tensile Strength (MPa)	65.0	55.7	31.8	51.1	75.2
Tensile Modulus (GPa)	2.8	2.8	1.26	3.6	4.10
Flexural Modulus (GPa)	2.2	1.6	0.82	3.3	3.7
Elongation at break (%)	6.2	24	49	2.0	5.6
IZOD Impact Strength (J/m)	25	38	109	14	N/A

1.2. 3D Printing with Composite Materials

As the neat resin systems for 3D printing do not provide mechanical properties sufficient enough for structural applications, recently, fiber reinforcement of the 3D printable resin systems are being studied. These fiber reinforcements can be short fibers or long continuous fibers. Continuous fiber reinforcement favors the longitudinal properties of the parts compared to the parts with short fiber reinforcement [26]. FDM technology has seen the most development of fiber-reinforced printed parts compared to other 3D printing techniques. FDM printing can print with short and long fiber reinforcements [27]. More work has been done in the literature to improve short fiber reinforcements compared to long fiber reinforcements. Both short and continuous fiber-reinforced thermoplastics are studied with FDM 3D printers [28-30]. For continuous fiber reinforcement in FDM printers, nozzle impregnation [18, 31, 32] and pre-impregnation [33-35] of polymers have been studied.

Because both SLA and DLP print thermoset resins from a liquid resin VAT, short fiber reinforcement is easier to execute in these methods of 3D printing. Different aspects of short fiber reinforced SLA and DLP prints have been conducted. Due to random orientation of the fibers and low fiber volume fraction (V_f), short fiber reinforced thermoset SLA prints show limited mechanical properties [36-38]. A fair amount of research on the alignment of short fibers in the printed body can be found in the literature [39-42].

Continuous fiber-reinforced composites offer improved mechanical properties, but 3D printing continuous fiber-reinforced composites is challenging, and studies involving 3D printing with continuous fiber reinforcement are minimal [43]. A comparative study was conducted for the performance of SLA 3D printed composites reinforced with particle, short and long fiber [26]. The quality finish was missing in the fabric-reinforced composite prints in this study. 3D printing of

wind turbines using electron beam cured epoxy reinforced with continuous carbon fiber (CF) was also studied and characterized [44]. These 3D printed parts suffered from poor interlaminar adhesion. The effect of compaction on interlaminar adhesion was studied to improve mechanical properties of 3D printed components [45, 46]. A similar study was conducted by pre-impregnating the fiber tow with heated epoxy resin and incorporating the epoxy's thermal melting in the printing nozzle [47]. In different studies [47, 48], experiments were conducted on the parameter optimization of this 3D printing approach. Inkjet 3D printers also utilize UV curable resin. Inkjet 3D printing can achieve high-resolution prints with multiple materials [49, 50], but the increased viscosity due to reinforcement makes it difficult to push the resin through the nozzle system [51]. The effects of different parameters on the final properties of inkjet 3D printed components were studied [52]. Rather than pushing the fiber tow, a pultrusion type mechanism for epoxy reinforced CF 3D printing was also studied by [17, 49, 52, 53]. A thermoset vitrimer resin was dispensed along with continuous fiber reinforcement by heating and melting the resin at the print head [53]. This approach produced 3D printed composite with high fiber volume percentage.

A different approach of resin infusion into continuous fiber-reinforced 3D printing is also being explored. Investigation of dynamic capillary action depending on the temperature gradient of the CF to control the epoxy infusion in the fiber tow [54] was conducted. This study concluded that a higher temperature gradient facilitates better resin infusion in the CF tow. Magnetic compaction force was studied for better infusion of matrix and fiber in the printed part [55]. Bi-matrix-infused CF composite was studied [56]. This study compared different modes of simultaneous infusion of two different matrix materials.

A nozzle mechanism was developed to push out continuous fiber by the sheer force of the resin flow for 3D printers [57]. Recently, Continuous Composites Company [58] developed a

prototype printer to print with continuous fiber-reinforced prints. Recently 3D printing with pre-impregnated continuous CF tow was studied [59]. This study utilized both UV and thermal curing to the print. This study was conducted with 1K pre-impregnated CF tow to achieve maximum resolution of 1 mm. Around 7% V_f was achieved in the final printed components.

The literature review on continuous fiber-reinforced 3D printing approaches shows that very few studies have been conducted in this field and even fewer utilizing thermoset resin systems. Moreover, almost all the studies that experimented with continuous CF reinforced thermoset resin composite utilized 3K or higher count CF. To improve the printing resolution, 1K CF (the thinnest CF tow available) tow was utilized in this research. Additionally, continuous fiber-reinforced thermoset 3D printing studies focused on utilizing an epoxy-based resin system. This study tried to modify commercially available acrylate-based 3D printable resin systems. This research work tried to develop a solution to prepare the reinforcing tow by formulating a prepreg. Hardware and software were developed for the 3D printer, solely focusing on the ability to handle continuous fiber reinforcement. Different print parameters were experimented with, and the printing process's performance with varied parameters was observed. The change of mechanical properties of the printed specimens characterized and the change of properties was correlated with the change of print parameters.

2. OBJECTIVE

The main objective of this project was to develop a 3D printing process that can print continuous fiber-reinforced thermoset polymer composites and study the effect of different print parameters. The fiber tow was pre-impregnated with resin before feeding into the 3D printer. So, pre-impregnating equipment was constructed to perform the fiber tow to prepreg conversion. The objective of this study was divided into the following parts-

- Building a 3D printer hardware and software that can print with continuous fiber-reinforced UV curable thermoset polymer.
- Construction of a prepreg producing machine that pre-impregnates resin into fiber tow and partially cure it for better printability and improved mechanical properties.
- Study print performance of different dispensing nozzle sizes by investigating surface topography and fiber volume percentage of the printed specimens.
- Try to improve print quality and their mechanical performance by optimization of printing process parameters, i.e., line spacing and resin flow rate ($\dot{V}_r$) for each nozzle configuration to find out maximum
- Mechanical and thermal characterization of 3D printed parts produced with different printing parameter configurations.

3. COMPONENTS OF THE 3D PRINTER

This project aimed to custom-build a 3D printer and its dedicated hardware and software. A gantry system was constructed using the X and Y movement arms from a repurposed gantry system. The Z movement of the nozzle was placed at the XY scanning arm. The fiber and resin feeding system was also placed in the printing arm. The control circuitry and the software were parallelly developed and integrated, focusing on the demand of continuous fiber prepreg handling and feeding it into the print. Figure is a 3D visualization of the printer components arrangement.

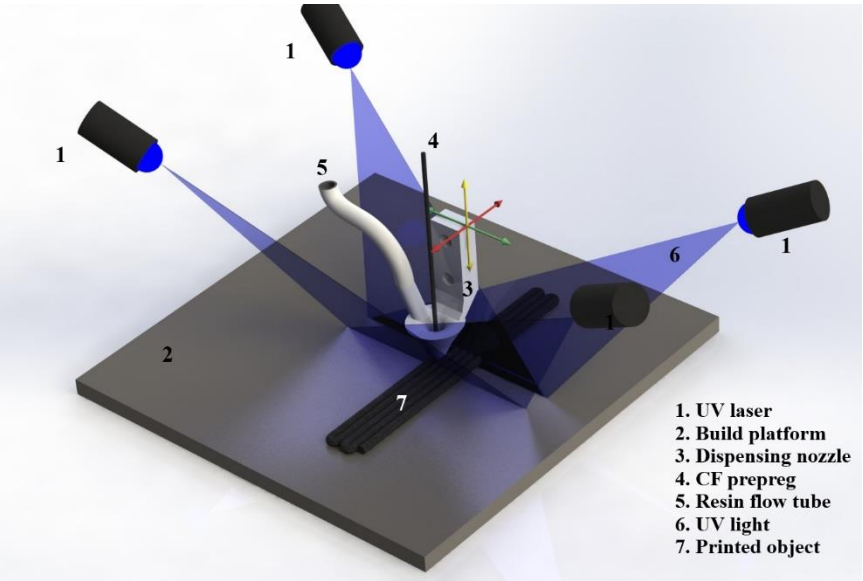

Figure 1: Schematic of printer components

3.1. Gantry System

The printing nozzle moves in X, Y, and Z directions with the gantry system. Gantry development was guided by early issues encountered during trials. The travel distance was 350 mm, 200 mm, and 20 mm for the X, Y, and Z directions. The X and Y direction was controlled by belt drives and the Z axis motion was controlled by screw drive. All three axes motion was driven by individual bipolar Nema 23 stepper motors (P Series Nema 23 Bipolar 1.8deg, 1.9 Nm, 2.8A 57x57x76 mm. 4 Wires). When the laser beam illuminates the UV curable liquid resin, the resin

reacts and solidifies in the printing approach. The solidification process produced slight shrinkage and warpage of the printed parts. The dispensing and curing sequence occasionally formed irregular clumps, eventually solidified by the laser beam. Besides, when the printing path executed the 180° turns, the fiber slightly bent upward, which resulted in bumps at the ends of the printed layers. These led to occasional interference between the printed object's top surface and the dispensing nozzle. This interference could damage or snap the prepreg. The dispensing nozzle was positioned under a preloaded vertical spring to reduce the detrimental effects of interference. This modification around the traditional printing arrangements allowed the printing nozzle to adapt and glide over occasional irregularities on the printed surface.

A flexible steel sheet was utilized as the build-plate for the prints. The build plate was chosen to be flexible in order to facilitate ease of removal of the printed objects. The metallic build plate was magnetically held flat on the platform. Strong niobium magnets were used to counteract the warping force generated from the shrinkage of the resin curing process. The build plate sat on 4 levelling screws. To further help the easy removal of the printed objects from the build plate, a coating of 3D printing bed glue was applied on the build plate before initiating the print. Figure 2 shows the working composite 3D printer.

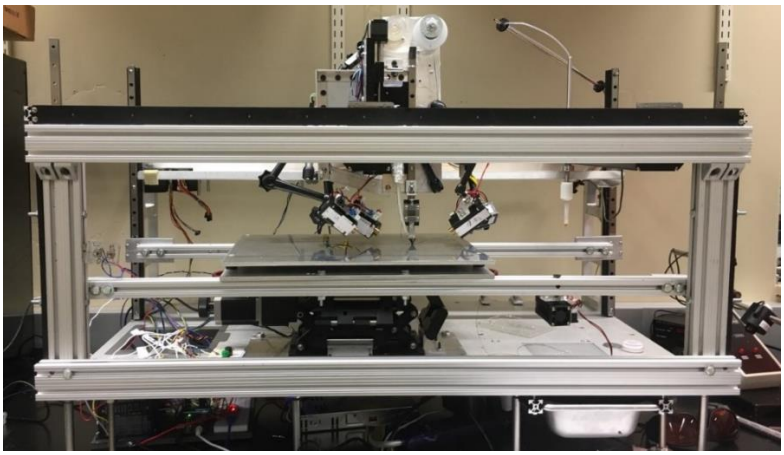

Figure 2: Custom built gantry system

The control circuit for the 3D printer was developed based on an Arduino controller (Arduino, Model: Mega2560 Rev 3, Microcontroller: ATmega2560). The printing process was able to pause within the print, and the Z height was adjustable while the printing process was paused. This feature allowed manual resetting the damaged or snapped tow through the printing nozzle. At the incidence of snaped or damaged fiber tow during the printing process, the printer was paused, and the print nozzle was lifted. The fiber tow was manually rerun through the nozzle, and then the print was resumed after the nozzle had been lowered to its printing height. As the controller code was written entirely from scratch, it allowed the process to be tuned for many printing parameters as needed. The controller code is provided in Appendix D.

3.2. Lasers

The print head had four lasers (two at each X-axis direction). Each laser is a 150 mW, 405 nm wavelength UV laser (Brand: F-Yi, 405 nm 150mW). The laser beam incident points on the print are located at a distance of 3 mm from the nozzle outlet tip. The lasers line width was 1mm at the curing spot. Distance between print bed and laser source was set at 150 mm. The print speed is tuned to provide the liquid resin with enough gelling time. The minimum gel timing varied with the amount of resin and thus the nozzle size. This tuning for print speed was accomplished by trial and error in the printing process. Details about the trial-and-error process are discussed in Section 7. Laser focusing was essential in this printing process. In the event of inaccurate laser positioning and spot dimension, the scattered UV cured the resin at the nozzle tip. This incident changed the nozzle shape resulting in several problems, i.e., interference with print, changing resin flow path, and snapping of the fiber tow. One possible solution to this was to place the laser focus away from the nozzle tip, but that adversely affected the resolution of the print, and the printer's capability of executing proper 180° turns at the end of each line. For these reasons, as shown in Figure 3, line

focusing of the lasers was chosen instead of dot focusing. The offset of laser lines from the nozzle tip was set at 3 mm for printing all the final test specimens.

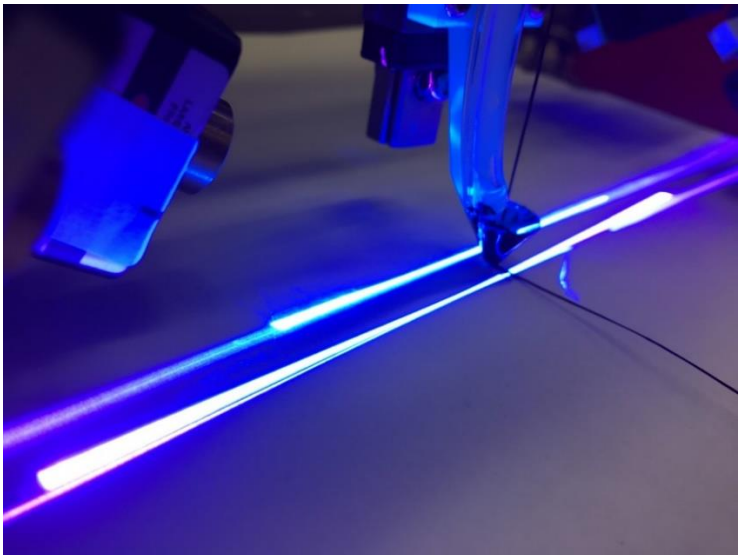

Figure 3: Laser positioning. Four lasers, each focused as a straight line
Figure note: ±x directions have two overlapping UV lines.

As mentioned earlier, the laser exposure point follows the dispensing nozzle of the printer at an offset distance of 3 mm. Due to design and process constraints, the lasers were mounted from each side of the printing line, and the laser lines were set perpendicularly to the printing line. Due to the shadow cast by the CF tow, this arrangement resulted in uncured resin underneath and on the opposite side of the prepreg when one laser line was assigned to follow the dispensing nozzle. The uncured resin's location at shadowed region is shown in Figure 4. This uncured resin deteriorated the adhesion to the print and caused peeling off of the printed lines. Two lasers were used from both directions perpendicular to the print line to overcome this problem.

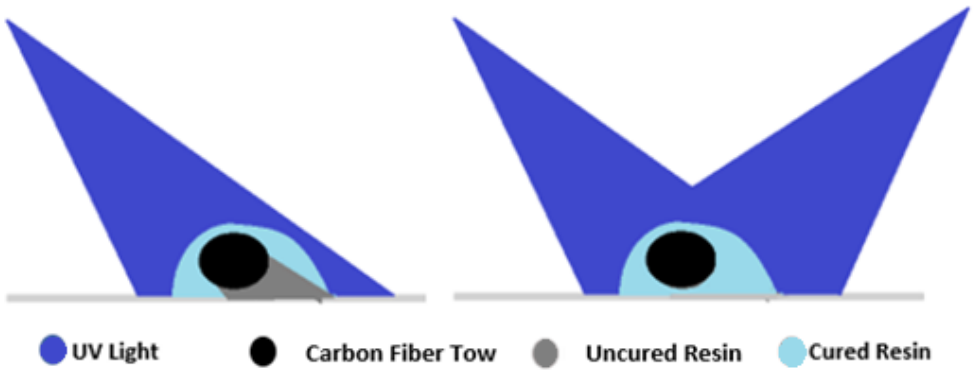

Figure 4: Depiction of shadow effect during the printing
Figure note: Left and right figures show one and two lases following the dispensing nozzle.

3.3. Material Delivery System

The prepreg tow was pulled through the printing nozzle by the tension from the print. Pre-calculated $\dot{V}_r$ to the nozzle was maintained during the printing process. The purpose of the resin pump was to provide the required amount of resin to the printing nozzle. From the nozzle, the resin was drawn out of the dispensing nozzle by the adhesion of the prepreg tow. During the initiation of the print, first, the prepreg tow was run through the nozzle and attached to the print bed by solidifying one dot 3 mm away from the nozzle tip. Then printing was ready to commence. As the print head moved, prepreg was pulled through the nozzle by the tension generated from the solidified points of the printed object. This draw of fiber prepreg carried the resin delivered to the nozzle by the resin pump through the exit tip. Figure 5 is the CAD drawing of the dispensing nozzle.

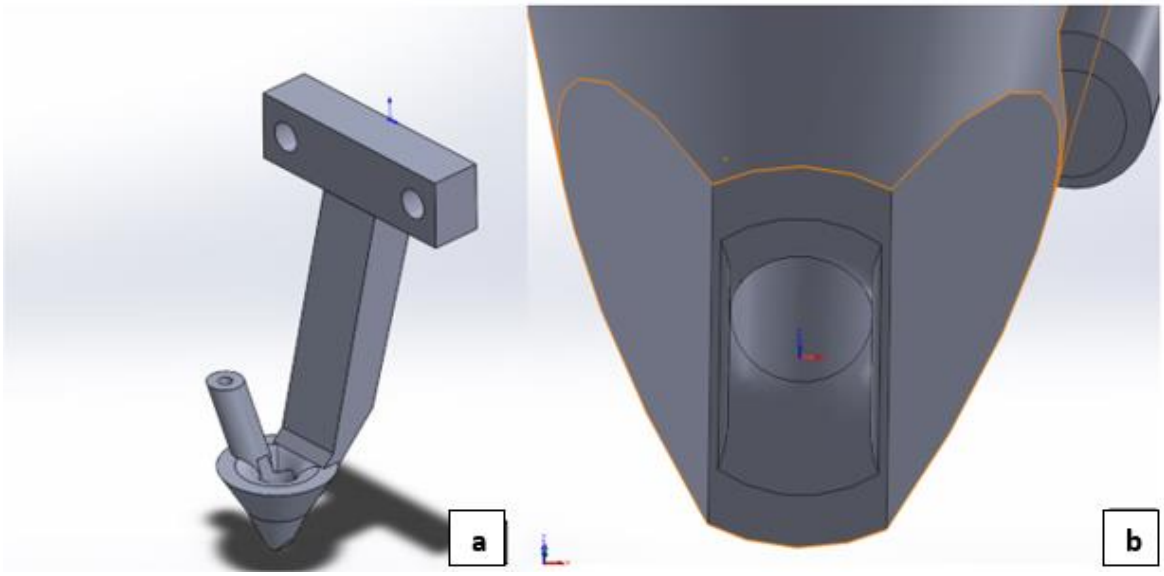

Figure 5: (a) 3D view of printer nozzle, (b) Tip of the nozzle
Figure note: The exit port has fillet only in ± Y directions.

The geometry and size of the nozzle are crucial aspects of the design. The nozzles of this composite 3D printer were 3D printed using a Formlabs 3D printer (Model: Form 2, Somerville, MA, USA, Resin type: clear V4). As shown in Figure 6, the nozzle system had two entries- one for resin and the other for the fiber prepreg. Fiber and resin came out together through the printing tip. As the resin was pushed into the nozzle, the excess resin had two exit routes: the fiber entry point and the dispensing tip. Resin flow through the prepreg entry was undesired as this could create additional drag to the prepreg movement and change the resin fiber flow balance. As the prepreg moved vertically through the nozzle and the print lines were horizontal, the prepreg went through a sharp right-angle turn at the exit of the dispensing nozzle tip. At this right-angled turn, the prepreg suffered from the detrimental drag and shear forces. These forces had damaging effects on the prepreg resulting in filament accumulation in the nozzle. The filament accumulation redirected the supplied resin toward the prepreg entry port. This occurrence could be troubleshot by observing any resin accumulation at the funnel-shaped portion of the dispensing nozzle. 3D printed nozzles, with the specifically designed rounded edge at the exit tip, as depicted in Figure

5, were used to maintain a smooth flow of resin and prepreg. The diameter of the nozzle and the $\dot{V}_r$ through it was varied, and the print performance of the varied parameters was evaluated. Figure 6a, b, and d show the cross-section of printing nozzles.

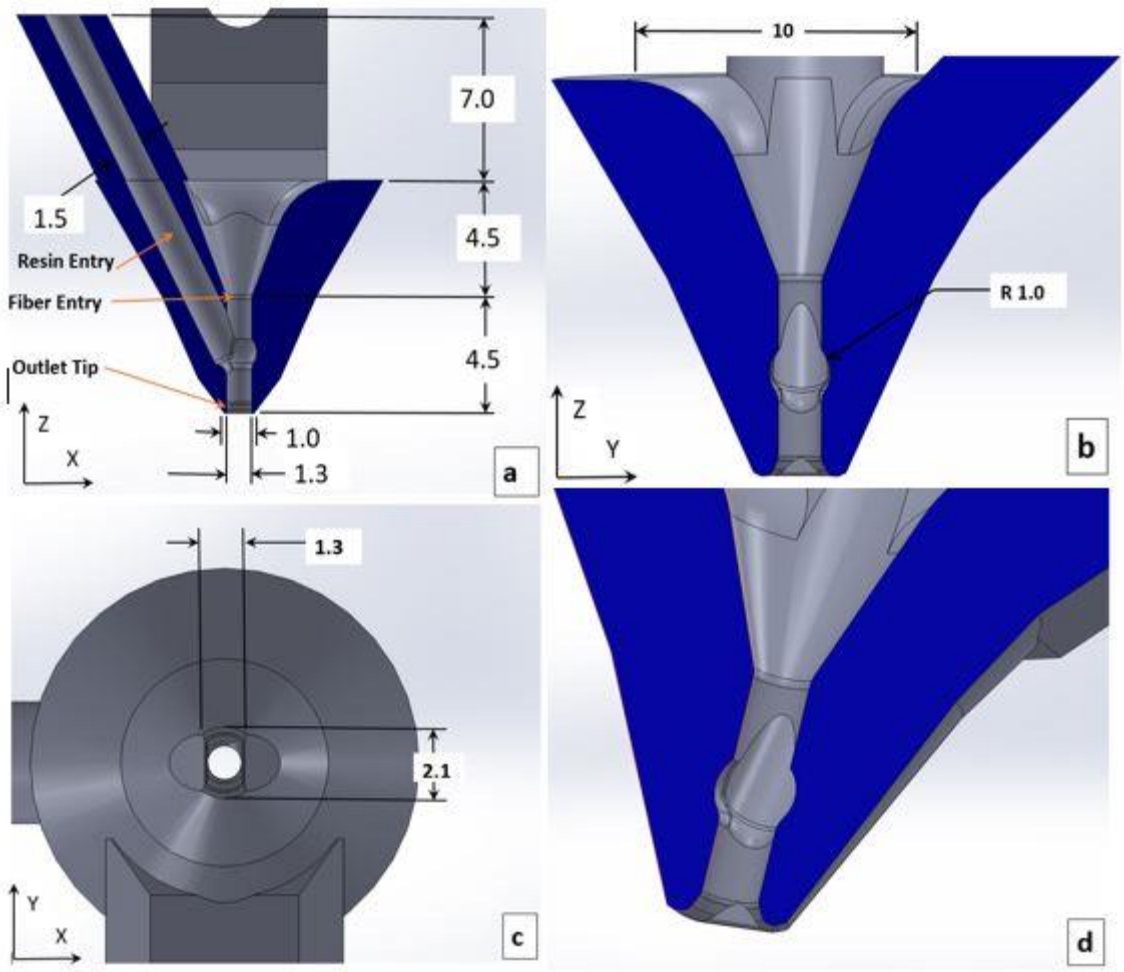

Figure 6: (a) Cross-section of printing nozzle in XZ plane, (b) Cross-section of the print nozzle in YZ plane, (c) bottom view of the nozzle tip, (d) 3D view of cross-section in XZ plane
Figure note: The dimensions are in mm.

The resin was pumped with a syringe drive. The syringe drive was driven by a screw dive, powered by a Nema 8 stepper motor (Stepperonline, Nema 8, bipolar, step 1.8 deg, 4 wire). It was controlled using an Arduino microcontroller (Arduino Nano A000005, ATmega328). The control code is provided in Appendix E.

3.4. Prepreg Production

The nozzles used to encapsulate the fiber tow with liquid resin, was designed with a small length (2 mm) fiber-resin mixing zone. This small length for fiber resin interaction is disadvantageous for resin impregnation into the fiber tow. It also establishes complications for variable print speed adjustment due to the resin flowrate dependency on fiber movement. Moreover, at higher print speeds, loosely packed fiber filaments suffered from tow damage at the nozzle tip. On the other hand, although a longer mixing chamber inside the dispensing nozzle facilitates better resin impregnation into the tow, it also adds additional drag force against the tow movement which can itself cause tow damage. To reduce the dependency of impregnation performance on print parameters, the resin impregnation into fiber tow was moved to an external preprocessing. This ensured the good resin impregnation. By partially curing the resin on the outer surface of the fiber prepreg tow was made resistant to fraying and damaging inside the dispensing nozzle of the printer. By this we essentially converted the CF tow into a prepreg. Figure 7 shows a schematic of prepreg production.

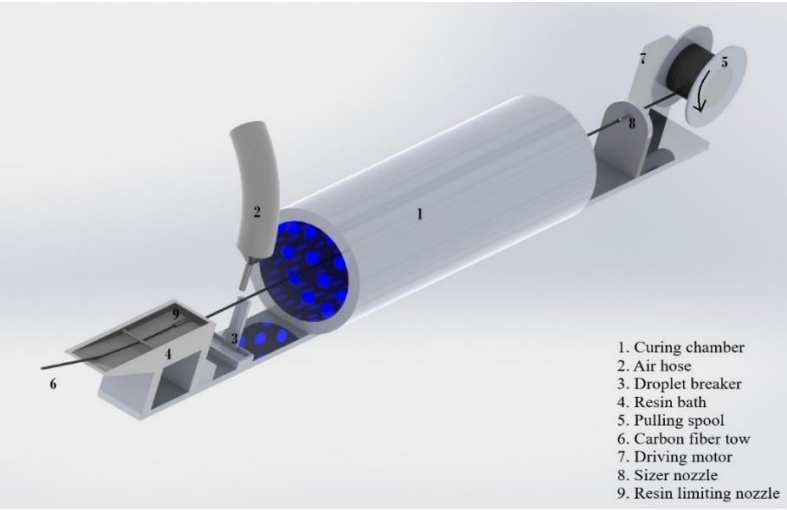

Figure 7: Schematics of prepreg production
Figure note: First syringe tip needle limits the amount of resin and the second one sizes the prepreg for 3D printer. The UV curing lights are 5V 405 nm wavelength LED. The chamber is 160 mm in length and 42 mm in diameter.

In this setup the tow is slowly pulled through a resin bath. This resin bath had the same resin that was used for 3D printing. The tow came out of the bath through a 0.603 mm inner diameter needle and ran over a scrapper. The purpose of this needle orifice is to limit the amount of resin that remains around the tow. The scrapper broke down the drop formations of resin around the prepreg. At the tip of the scrapper, an air blower removed the excess resin that came in the form of droplets around the prepreg. The pre-impregnated tow then ran through a curing chamber. The curing chamber is a cylindrical chamber, coaxial with the tow, with light emitting diode (LED) illumination. The LEDs in the curing chamber emitted light with 405 nm wavelength. This curing chamber illuminated the prepreg with 120 LEDs. The LEDs (Waygor 5V 120 LED Strip, China) were arranged in a cylindrical array (160 mm long x 42mm diameter). The light at the curing chamber partially cured the resin coating of the prepreg. The partial curing made the tow slightly rigid. Then the partially cured tow ran through another orifice. This orifice (0.686 mm diameter) is slightly larger than the first one (0.603 mm diameter) but slightly smaller than the 3D printer nozzle entry (0.8-1.2 mm diameter). The second orifice assured that the prepreg is appropriately sized for smooth pull through the printer nozzle. The prepreg was wound on a spool (35 mm in diameter). A DC motor drove this spool. The amount of resin on the tow dictates the properties of prepreg. This amount was controllable by variable pulling speed, airflow, and orifice sizes. The faster running speed of the tow resulted in an increased amount of resin drawn by the tow. The increased amount of the resin around the fiber tow made the prepreg less flexible at the end of the process. The resin volume fraction in the prepreg ranged between 23-62% in the fiber running range of 0.5-4 mm/s. This speed was finally adjusted to 1 mm/s with trial and error with printing consistency. At this fiber run speed the amount of resin in the prepreg was calculated to be ~33% (by volume).

The prepreg composition was investigated using a Keyence microscope (Keyence VHX-S750E, Osaka, Japan). The prepreg spool was completely cured by post-curing it at an elevated temperature to carry out this investigation. Then the spool's cross-section was investigated using the microscope (Figure 8). The quality resin impregnation into the CF tow was determined by checked by the microscopic image. In Figure 8 light grey circles are individual fiber filament. The dark grey zone is the matrix material. The black dots are polishing imperfections. [59]. Image generated using Keyence VHX microscope (Osaka, Japan).

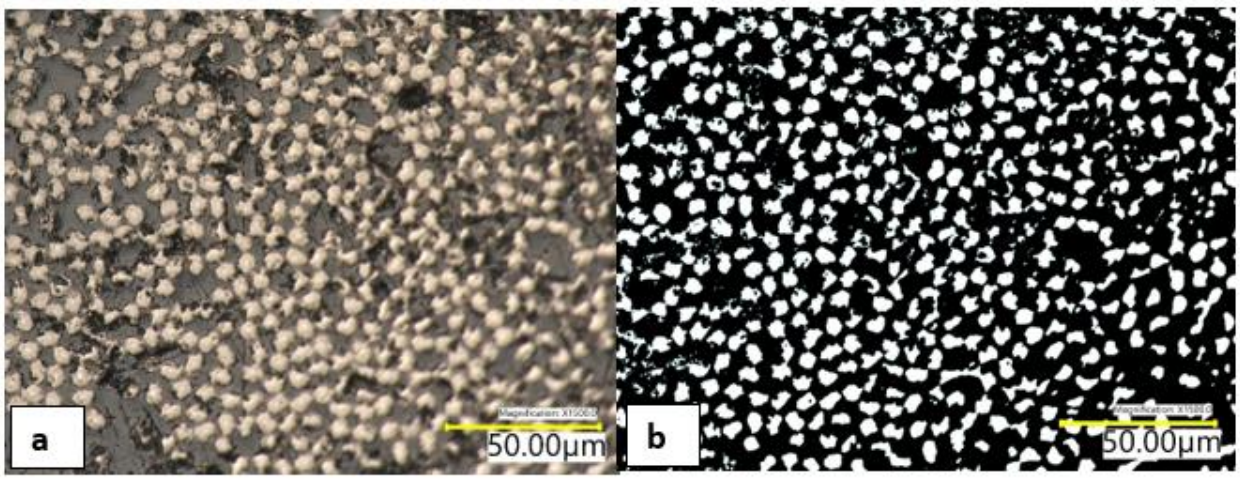

Figure 8: (a) Microscopic image of prepreg cross-section, (b) Monochromatic image of microscopic cross-section of prepreg
Figure note: (a) Light and dark areas are fiber and matrix, respectively. (b) Black and white area are matrix and fiber, respectively.

4. MATERIALS

The study focused on constructing a 3D printer that will be adaptive to a wide range of materials. The design considerations, while construction of the printer, prioritized usability of from-the-shelf commercial UV curable resin systems and the novel resin systems developed by the NDSU Coatings and Polymeric Materials department. The fiber handling capabilities of this 3D printer were designed to be tunable for different types of continuous fiber tows, such as CF, basalt, aramid, and glass fiber. One material combination was studied through printing to keep this study concise. For greater strength values of 3D printed composite, CF tows were chosen for reinforcement. To attain the sharpest print resolution, the CF tow count was chosen to be 1K. This 1K CF was graciously provided by TORAY (Toray, Type T300, Filaments 1000-40A, TorayCA, Washington, USA). The material properties of this CF are listed in Table 2.

A UV curable resin from Peopoly (type: deft white, Peopoly, California, USA) was used as a matrix material. This is an Acrylic based resin. The chemical composition of this resin is 20-30% Urethane Acrylate, 30-70% Acrylic monomer, and less than 5% photoinitiators. The resin system is cured at the exposure of 405 nm wavelength light. This resin did not cure appreciably with the addition of thermal energy. This led to introducing a thermal initiator to the Peopoly resin for proper matrix curing with additional heating.

Table 2: Material properties [60, 61]

Property	Toray 1K CF	Peopoly deft resin
Tensile strength (MPa)	3530	35
Tensile modulus (GPa)	230	.75
Elongation (%)	1.5	6
Density (gm/cm^3)	1.76	1.15
Viscosity (cps at 25^o C)	-	105

In this study, Luperox P was mixed, as a thermal initiator, with Peopoly clear resin at 2% by weight. The Peopoly resin and Luperox P (tert-butyl peroxybenzoate 98%, Sigma-Aldrich Saint Louis, MO, USA) are mixed in a centrifugal mixer, shown in Figure 9a, (Hauschild Engineering, Model: SpeedMixer, Type: DAC-150 FVZ, Water camp, Germany) using 1500 RPM for 2 minutes. Then the mixture is degassed in a vacuum chamber, shown in Figure 9b, (Sheldon Manufacturing INC, Model: 1415M, Cornelius, OR, USA) for 15 mins using -85 kPa. This mix was used for both prepreg formation and printing processes.

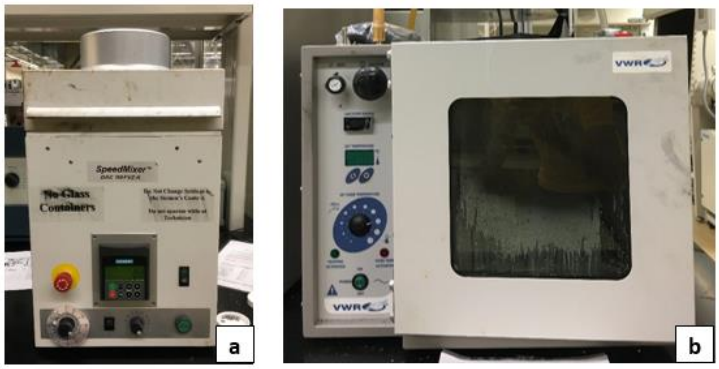

Figure 9: (a) Speed mixer, (b) Vacuum oven
Figure note: Only the vacuum function was used for degassing at room temperature.

5. PRINTING OF SAMPLES

5.1. Printing

Composite rectangular bars were printed for mechanical property characterization and print quality evaluation. Each bar consisted of six layers of composites reinforced with longitudinally unidirectional CF. Figure 10 shows a schematic of the printing process and the laser sequence depending on the direction of print head movement. As mentioned earlier, at the end of each line, the fiber had to make a 180° turn, which made the fiber bend upward a little. These small bumps at the layer boundary compounded with each layer and eventually led to the interference of the nozzle and the print body. This interference caused the failure of the printing process. To avoid this interference, every new layer's length was shortened at both ends. This practice gave the ends a stair-like structure and stopped the nozzle from interfering with the bumps at the ends. So, by this method, the stair-like edges functioned as anchoring zones to continue the CF for each new layer. The layers arrangement is shown in Figure 11(b).

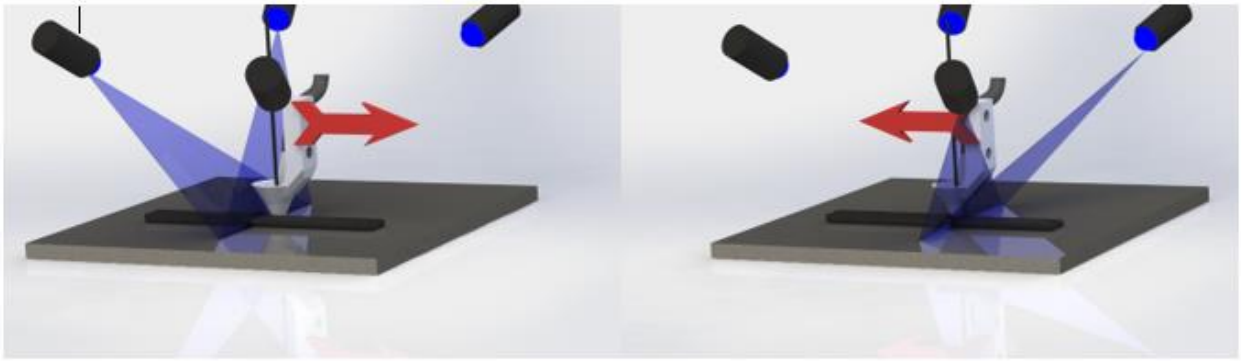

Figure 10: Laser illumination sequence
Figure note: Two sets of UV lasers turn on and off depending of the travel direction of print head.

One of the major factors that dictate the mechanical properties of the printed composite bar is the fiber volume fraction, V_f. The printed parts should have a high V_f for the composites to have fiber-dominated mechanical properties. In this study, process parameters were altered, targeting

incremental changes of V_f in the continuous fiber-reinforced 3D printed objects. This was achieved by bringing the printed lines closer to each other. To pack the tows in a tight space, the amount of matrix material between them should be precisely calculated. The amount of resin coming out with the fiber depends on the pumping rate, print speed, and nozzle diameter. The nozzle diameter and print speed affected the amount of resin output because of the orifice of the fiber entry port. Excess resin pumping results in the backflow of resin through the fiber entry orifice. Due to the viscosity of the resin used in the printing, the speed of fiber tow movement alters the amount of resin it carries with it in print. So, in the experiment, nozzle diameter, resin pump rate, and line spacing were selected as the control variables for optimization. The line spacing was the distance between the centerlines of two adjacent print lines. Figure 11(a) shows a composite specimen being printed.

To determine the tightest packing achievable with this 3D printer, a large diameter nozzle (1.2 mm inner diameter) and wide line spacing (1.2 mm) are selected for the initial parameter configuration. Printed samples with this configuration are shown in Figure 11(b). These values were selected based on a previous study [59]. The line spacing is gradually reduced from this initial configuration until the setup fails to print. Then the same iteration was carried out with a reduced nozzle size. By this, the study attempted to converge to a setting for high value of V_f in the printed composites. More on this is discussed in Section 6. After completion of the printing process, the printed parts were post cured in elevated temperature in an oven.

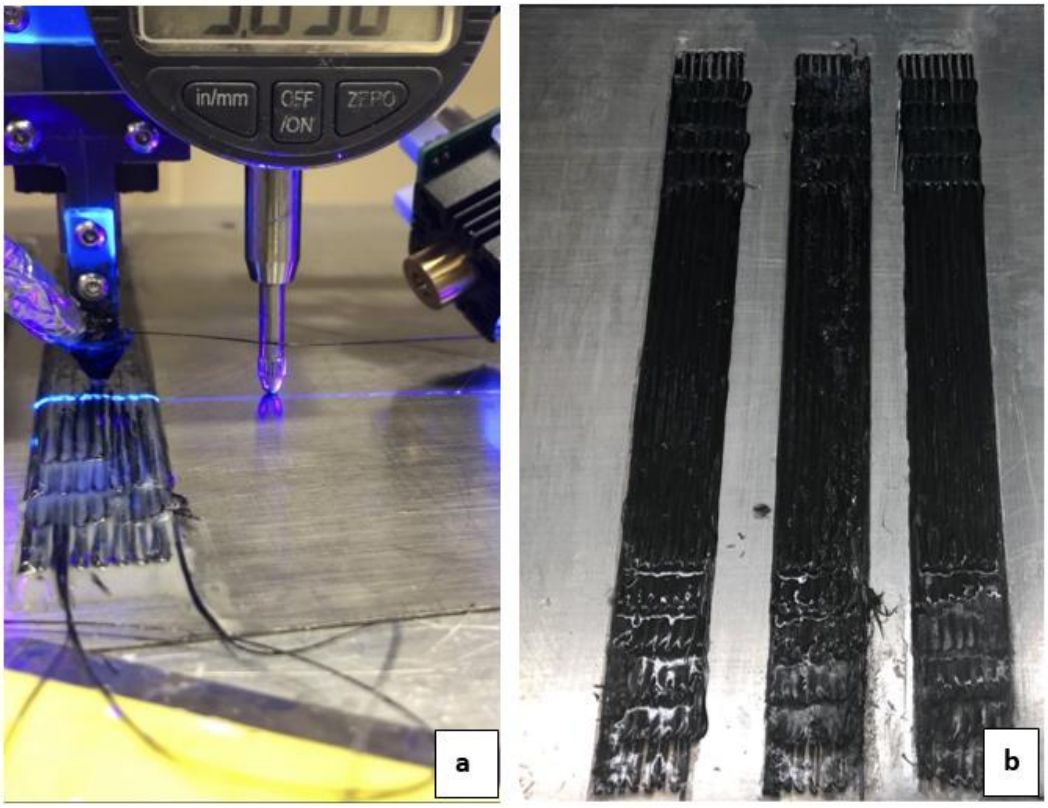

Figure 11: (a) Composite specimens being printed, (b) Composite rectangular bars
Figure note: Samples in these figures were printed using 1.2 mm nozzle with 1.2 mm line spacing and 180° turns at each end.

5.2. Postcure

CF is opaque to UV light. 3D printing with UV curing does not cure the resin fully at the shadowed part of the tow. The resin is mixed with a thermal initiator (tert-butyl peroxybenzoate) to achieve complete curing inside the printed objects. The printed parts were postcured in an oven at 130 °C for 1 hr 30 min [59]. A VWR oven (VWR, Sheldon Manufacturing INC, Model 1350FM-2, Cornelius, OR, USA), shown in Figure 12, was used for the postcuring process.

Figure 12: Postcuring oven

6. OPTIMIZATION OF PRINT PARAMETERS

The effect of changed print parameters on the mechanical properties of printed objects and printing process performance were investigated in this study. Process optimization was studied to analyze the change in performance with varied print parameters. The selected parameters for optimization were, dispensing nozzle diameter, $\dot{V}_r$, and line spacing. Idealistically, increased fiber content improves the mechanical properties of the print. Nevertheless, the prepreg tow needed a minimum amount of resin as a matrix material for a consistent and reliable printing process. So, the study tried to converge to the maximum fiber content recipe with consistent printing performance and then investigate the mechanical property offered by that recipe. The amount of resin was dictated by several factors, i.e., the filament count and diameter of the prepreg tow, spacing between the print lines, speed of the printing, diameter of the printing nozzle, shape of the tip of the nozzle, viscosity of the resin. As mentioned in an earlier section, this study investigated the print parameters utilizing 1K CF tow for maximum achievable resolution. To study the effect of these printing parameters, a test matrix was created and is presented in Table 3.

Table 3: Test matrix for the processing parameters

	1.2 mm	1.0 mm	0.8 mm
Max spacing	Spacing=1.2 mm Layer thickness=0.4 mm Resin flow=4.81 cc/hr	Spacing=1.0 mm Layer thickness=0.4 mm Resin flow=3.95 cc/hr	Spacing=0.8 mm Layer thickness=0.4 mm Resin flow=3.37 cc/hr
Intermediate spacing	Spacing=1.1 mm Layer thickness=0.4 mm Resin flow= 4.5 cc/hr	Spacing=0.92 mm Layer thickness =0.4 mm Resin flow=3.62 cc/hr	X
Minimum spacing	Spacing=1.0 mm Layer thickness=0.4 mm Resin flow=4.29 cc/hr	Spacing=0.85 mm Layer thickness =0.4 mm Resin flow=3.62 cc/hr	Spacing =0.75 mm Layer thickness=0.4 mm Resin flow=3.37 cc/hr

The diameter of the nozzle was significant for the printing process. The diameter of the nozzle dictated how much resin was required to be pumped around the fiber tow. As the tow count and print speed were kept constant, the larger diameter of the nozzle required more resin. Nozzle size also dictated the line spacing of the print. Intuitively, the printed adjacent line's centerline should be spaced at a distance equal to the nozzle diameter. However, as the resin was dispensed at a liquid state around the prepreg, due to the liquid state resin dispensing, the printed line's top surface produced an arched surface (Figure 4). This resulted in a waviness on the top surface of the printed layer. This waviness compounded with each layer and ultimately created void zones in print. Therefore, printing was executed with print lines placed as close as possible to reduce the valley in two adjacent print lines. The resin flow rate into the printing nozzle, $\dot{V}_r$, was balanced depending on the line spacing.

As shown in the test matrix (Table 3), three nozzle diameters (1.2, 1, 0.8 mm) were selected for the optimization. It has been observed that printing with nozzle diameter smaller than 0.8 mm damaged the prepreg resulted in frequent prepreg breakage during the 3D printing process. Composites were printed with different line spacing for selection of each nozzle size. The max and minimum line spacing for each nozzle were dependent on the diameter of the nozzle used for that configuration. The maximum line spacing was selected to be equal to the diameter of the selected nozzle. Minimum line spacings possible for each nozzle size were found out by trial and error. After setting up the spacing boundaries, intermediate spacing configurations were also tested for print performance (except for the 0.8 mm nozzle). The closest spacing achieved for printing was 0.75 mm. For 0.8 mm nozzle no intermediate line spacing was tested as the difference between maximum and minimum spacings for 0.8 mm nozzle was very small.

The resin pumping rate into the nozzle was a dependent yet important process parameter. The rate of resin required is dependent on the layer thickness, raster spacing, and the speed of printing. Depending on the other parameters, the $\dot{V}_r$ was adjusted to a rate that resin only exits through the outlet tip of the dispensing nozzle, and there was no resin backflow through the fiber entry port. This backflow could disturb the desired mass flow ratio into the print and induce increased drag to the fiber. $\dot{V}_r$ depended on the print speed because the tow carries resin to the print by viscous adhesion. The mass flow equilibrium with no backflow was calculated from Equation 6.1. Here d_N & d_F are nozzle and tow diameters, respectively and s is printing speed. Now considering the area under the cross-sectional profile curve (Figure 4) as A, Equation 6.2, can be formulated. Equation 6.2 relates the printing parameters with the topographic data. Equation 6.1 & 6.2 are formulated based on the assumption of no void in the print body.

$$\dot{V}_r = \frac{\pi}{4}(d_N^2 - d_F^2)s \tag{6.1}$$

$$A = \frac{\dot{V}_r}{s} + \frac{\pi d_N^2}{4} \tag{6.2}$$

The effects of variable print spacing, nozzle size, and $\dot{V}_r$ were studied to optimize parameters. For better packing the fiber tow in the composite, it was essential to study the topography of the printed lines. This was done by using a KEYENCE VHX digital microscope. Figure 13 shows the microscope-generated topographic profile of the top surface single layer print. To quantitatively rank the quality of printed layers, the surface roughness (S_a) was measured using different parameter configurations. S_a was tested under 40X enlarged microscopic imaging. To filter out the noise and general waviness of build-platform, the cutoff wavelength of roughness measurement was set from 100 µm to 2.5 mm. The fluctuations outside this wavelength range were filtered out. S_a was calculated using Equation 8.1. Details about topographical study is discussed in Section 8.1.

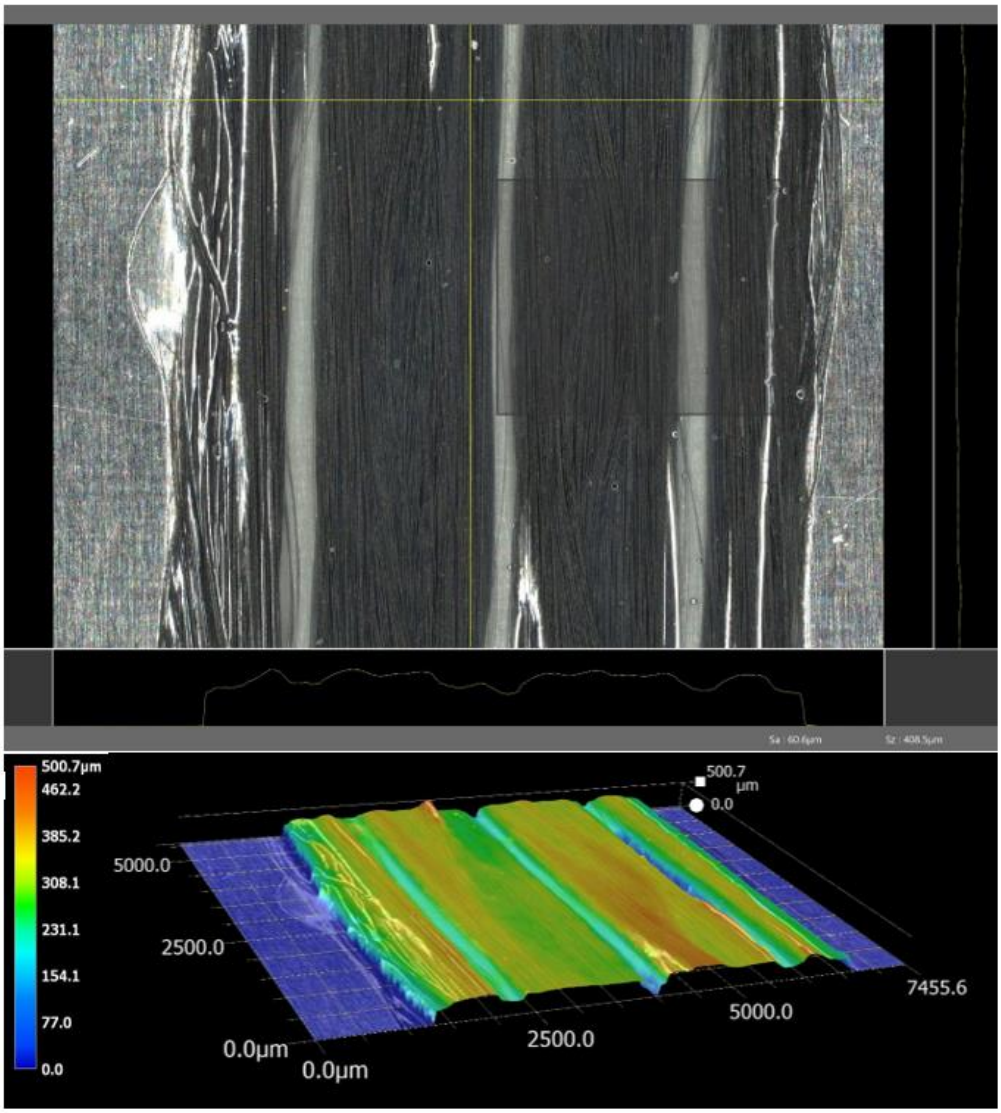

Figure 13: Topographic analysis of printed surface

The $\dot{V}_r$, nozzle size, line spacing, and print speed are interconnected and dependent on each other. Multiple combinations of the parameter changes can achieve the desired change in print performance. To streamline the study, adjustments to print parameters were made according to the system diagram shown in Figure 14.

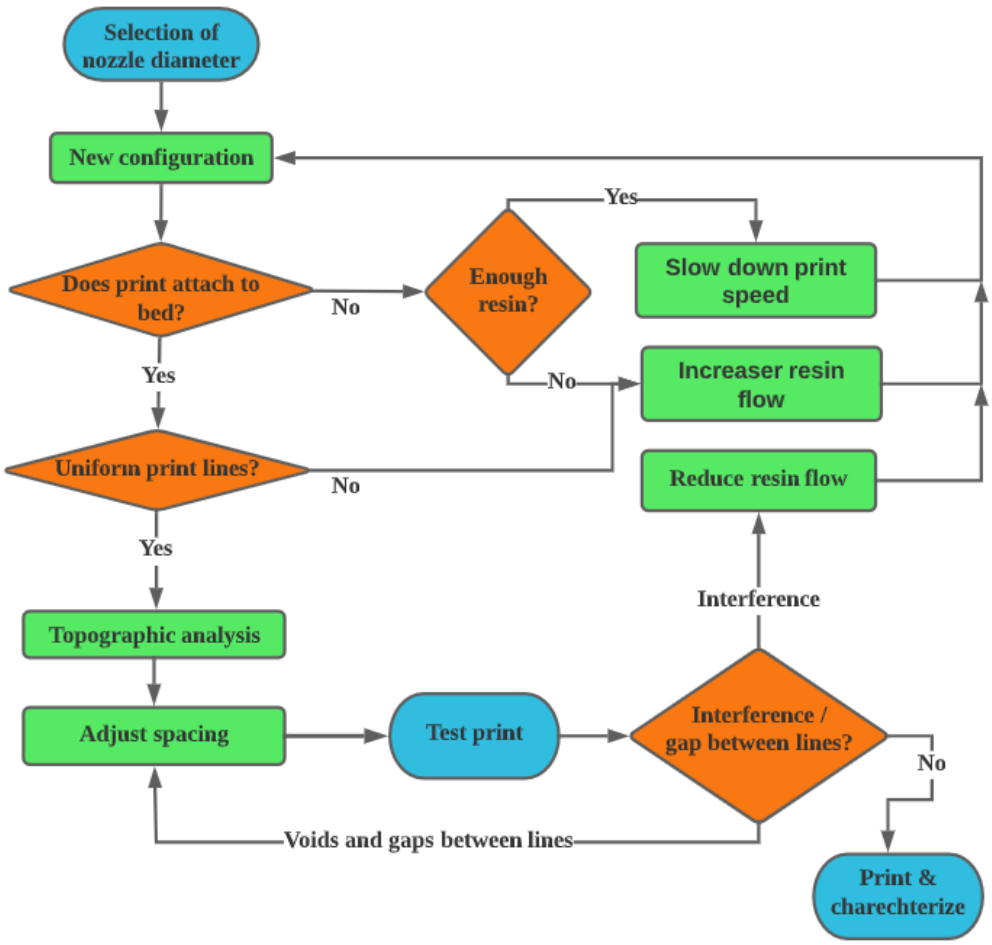

Figure 14: System diagram for parameter adjustment

7. TESTING

7.1. Tensile Test

Tensile properties of the 3D printed composites were tested by Instron load frame (Model 5567, Norwood, MA, USA). The Instron load frame with tensile configuration is shown in Figure 15. Tensile loads were measured using a 30 kN load cell, and strains were measured using a 25.4 mm extensometer. All tensile tests were conducted using the ASTM D3039 standard [62]. The specimens were printed as rectangular bars of a gauge length of 100 mm. The specimens' width and thickness were 11-19 mm and 2.4 mm, respectively. The crosshead displacement rate was 1 mm/min. For gripping of the tensile specimens, they were tabbed at both sides with glass fiber epoxy composite. Tabs were attached to the printed composite using two-part epoxy glue (Loctite, E-20HP). The load-displacement data from the tensile test were plotted, and tensile elastic modulus E was calculated using Equation 7.1. Here, σ_t and ε_t are tensile stress and strain, respectively.

$$E = \sigma_t / \varepsilon_t \tag{7.1}$$

Figure 15: Instron 5567 load frame in tensile test setup

7.2. Flexural Test

Printed composite flexural properties were tested with a 3-point bend test. Flexural tests were conducted to failure according to ASTM D7264 standard [63]. The span to thickness ratio of the samples was 32:1. Flexural tests were performed using an Instron load frame (Instron, Series: 5567, Norwood, MA, USA) with a 2 kN load cell. According to the standard, the crosshead movement was 1 mm/min. Flexural stress was calculated from Equation 7.2. Where σ_f stress in the outer fibers at midpoint, P is the load given at a point on the load-deflection curve, L is support span, b is width of beam, and d is depth of beam.

Equation 7.3 was used for calculating flexural strain ε_{fl} at the outer surface of the sample. Here D is the max deflection at the center of the beam and d is the depth of the beam. With the flexural stress and strain, flexural chord modulus E_{fl} were calculated using Equation 7.4. In this Equation σ_{fl1} and σ_{fl2} are flexural stresses measured at predefined points on the load-deflection curve, and ε_{fl1} and ε_{fl2} are flexural strains measured at predefined points on the load-deflection curve

$$\sigma_{fl} = \frac{3PL}{2bd^2} \tag{7.2}$$

$$\varepsilon_{fl} = \frac{6Dd}{L^2} \tag{7.3}$$

$$E_{fl} = \frac{\sigma_{fl1} - \sigma_{fl1}}{\varepsilon_{fl1} - \varepsilon_{fl2}} \tag{7.4}$$

7.3. Thermogravimetric Analysis

Thermogravimetric Analysis (TGA) investigated the printed composites' thermal stability. Thermal degradation temperatures were calculated from the TGA analysis. Knowing the thermal degradation temperature was important before conducting Dynamic Mechanical analysis (DMA) because the DMA equipment can be damaged if the specimen thermally degrades. The TGA test

was done according to ASTM E1131 standard. TGA tests were conducted using TGA Q500 (TA Instruments, Series Q500, Eden Prairie, MA, USA) shown in Figure 16.

Figure 16: TGA Q500

7.4. Dynamic Mechanical Analysis

Dynamic Mechanical Analyses (DMA) was performed to characterize printed composites' viscoelastic properties. DMA of a dual cantilever composite beam was conducted using a Discovery DMA 850(TA Instruments, Eden Prairie, MA, USA) equipment shown in Figure 17. The tests followed ASTM D7028 [64] standard. The glass transition temperature, storage modulus, and loss modulus were obtained from the DMA analysis. The effect of V_f on the glass transition temperature was investigated.

Figure 17: Discovery DMA 850

7.5. Burnoff Test

Burnoff tests were conducted to determine the V_f of the printed composites. Small sections of the printed composites were cut out and placed in the Lucifer Furnace, shown in Figure 18, to burn off the matrix materials. The burnoff tests were completed in reference to ASTM D3171 [65] standard. The composite was heated at 565 °C for 6 hours in a nitrogen environment. From the mass difference of before and after burning off the matrix materials were used to calculate the V_f. The V_f data was then used to model and correlate the mechanical properties of the composite. Equation 7.6 was used to calculate the V_f. To calculate V_f, first V'_f (fiber volume fraction with assumption of no void) was calculated using Equation 7.5. Here, w_f and w_m are the weight of fiber and matrix in the composite, respectively. ρ_f and ρ_m are the density of the fiber and the matrix, respectively. Void fraction V_v was obtained from the microCT tests.

$$V'_f = \frac{\frac{w_f}{\rho_f}}{w_f/\rho_f + w_m/\rho_m} \tag{7.5}$$

$$V_f = \frac{V'_f}{1+V_v} \tag{7.6}$$

Figure 18: Lucifer furnace

7.6. MICROCT

The printed samples were tested in the Micro CT. The Micro CT tomographic images were analyzed for the fiber filament distribution in the matrix. The tomographic analysis was used to quantify the distribution and size of voids in the composite parts. The Micro CT was conducted using a GE Micro CT Scanning System, shown in Figure 19 (Model: Phoenix v|tome|x s, Fairfield, CT, USA), at the NDSU electron microscopy center.

Figure 19: GE MicroCT Scanning System [66]

8. RESULT AND DISCUSSION

8.1. Topographic Analysis

To find out the optimum amount of resin flow for each nozzle size and $\dot{V}_r$ configuration, topographic analysis of the printed surface was conducted. This analysis was carried out by measuring surface roughness (S_a) at the top surfaces of single-layer prints. As mentioned in the earlier section, S_a was measured using a Keyence VHX microscope. One layer of composite was printed with different $\dot{V}_r$ and print spacings for each nozzle size. S_a data was taken from the middle section of printed layers. The areas of interest were 5 mm long and six print lines wide. With the reduction of line spacing for a fixed $\dot{V}_r$, the S_a showed a decreasing trend. The most significant source of the S_a changes was the valley between two adjacent print lines because of insufficient resin in that region. As layer thickness was kept fixed, the valleys' depth could be reduced by either increasing the $\dot{V}_r$ or by decreasing the spacing between adjacent print lines.

The individual dimensions varied significantly for the peaks and valleys even in the surfaces printed with the fixed printing parameters. A significant reason behind this variability in the surface finish was that the deposition of solid and liquid materials at the print had inherent positional uncertainty. Moreover, the shrinkage of the liquid resin during solidification was somewhat indeterminate. So, printed specimens with seemingly optimized $\dot{V}_r$ and spacing could still have gaps and voids. However, this study tried to quantitatively measure the degree of optimization of $\dot{V}_r$ and line spacing by measuring the S_a. S_a values over an area A were calculated using Equation 8.1. In this Equation, $z(x, y)$ was the vertical distance of the surface profile at any point. The z distances were measured from the average surface profile. Average surface profiles were calculated through the least square method.

$$S_a = \frac{1}{A} \iint |z(x, y)| dx dy \tag{8.1}$$

The surface roughness provided a quantitative yardstick for setting up a threshold value for a print configuration to be assessed whether the configuration passed or failed for further specimen printing. Specimens printed with configurations that showed S_a lower than the set threshold were taken for mechanical characterization tests. The maximum threshold value for S_a was selected to be 60 µm. Figure 20 showed the plot of S_a values obtained from surfaces printed with 1.2 mm nozzles.

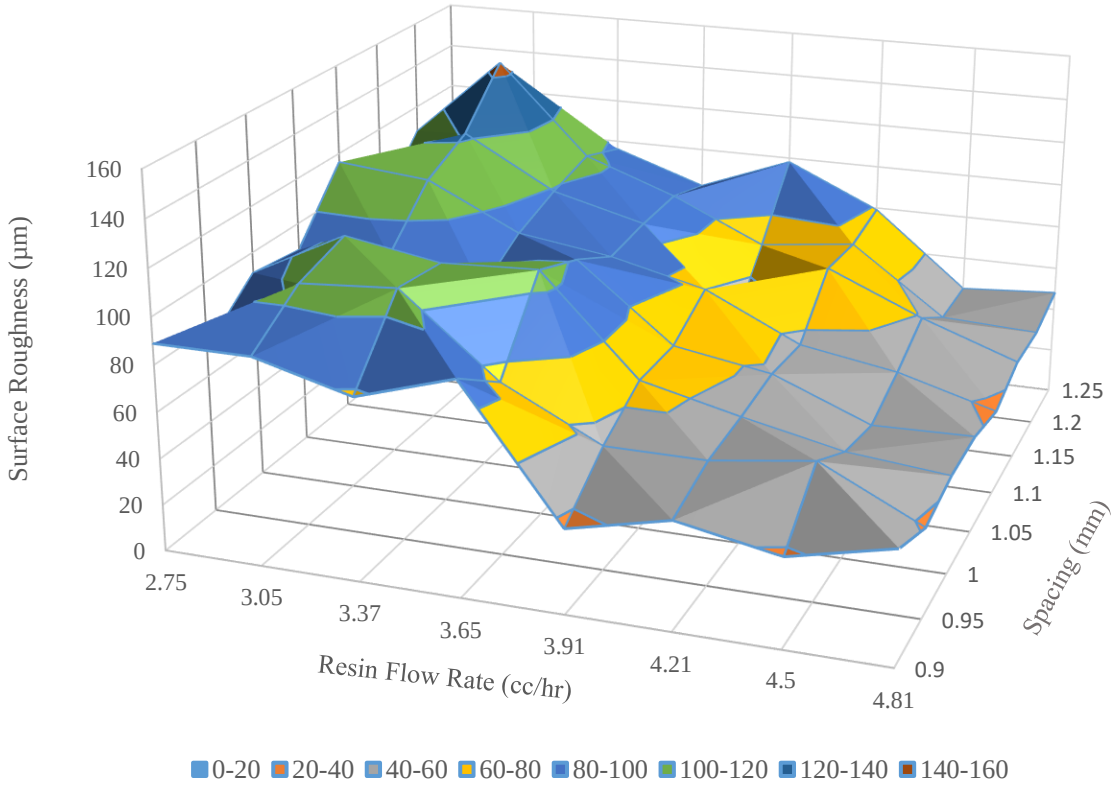

Figure 20: Surface roughness of single layers printed with 1.2 mm nozzle

Despite the fluctuations, the S_a values of surface printed with 1.2 mm nozzles exhibited a trend towards achieving a minimum value below 50 µm. From Figure 20, it is observed that surfaces printed with 1.2 mm nozzles and $\dot{V}_r$ above 4.21 cc/hr had S_a values below the maximum threshold limit of 60 µm. These spacing and $\dot{V}_r$ configurations are presented as the grey area in the

surface plot in Figure 20. To obtain maximum V_f, for a specific line spacing, $\dot{V}_r$ was chosen at the minimum value from where S_a was stably below the set threshold. For example, S_a values are stably under 60 µm for resin $\dot{V}_r \geq 3.91$ cc/hr. when 1 mm line spacing is used. So, to achieve maximum V_f, 3.91 cc/hr. resin flow rate is used for 1 mm line spacing with 1.2 mm nozzle. For any spacing (with 1.2 mm nozzle) the $\dot{V}_r$ were taken from the interfacial line between grey and yellow region of the surface plot in Figure 20.

While S_a varied significantly for configurations with 1.2 mm printing nozzles, S_a for 1 mm and 0.8 mm nozzles fluctuated within a narrower range of values. This difference in extreme limits of S_a values was observed because of the selection of tighter line spacings for smaller-sized nozzles. These selections of print settings left even slimmer space for the resin to occupy between the lines when small nozzle sizes were utilized. Figure 21 & 22 show the S_a maps for surfaces printed with 1 mm and 0.8 mm nozzles, respectively.

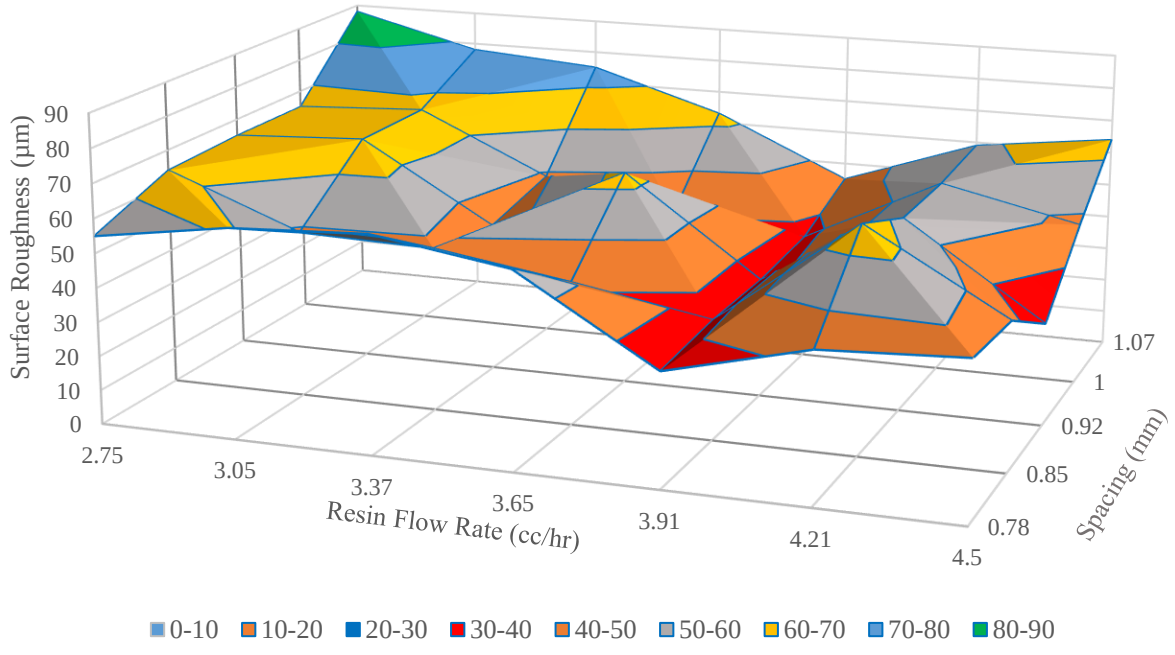

Figure 21: Surface roughness map for single layer prints with 1.00 mm nozzle

From Figure 21, it was observed that for $\dot{V}_r$ > 2.43 cc/hr, the surface roughness starts to increase again. This observation indicated that $\dot{V}_r$ had critical points for each nozzle size and spacing configurations. When $\dot{V}_r$ was set above this critical value, resin started to overflow around the nozzle outlet lips, thus increasing the roughness of the printed surface. This observation also indicated that the minimum surface roughness achieved by this 3D printing setup was ~30-40 µm.

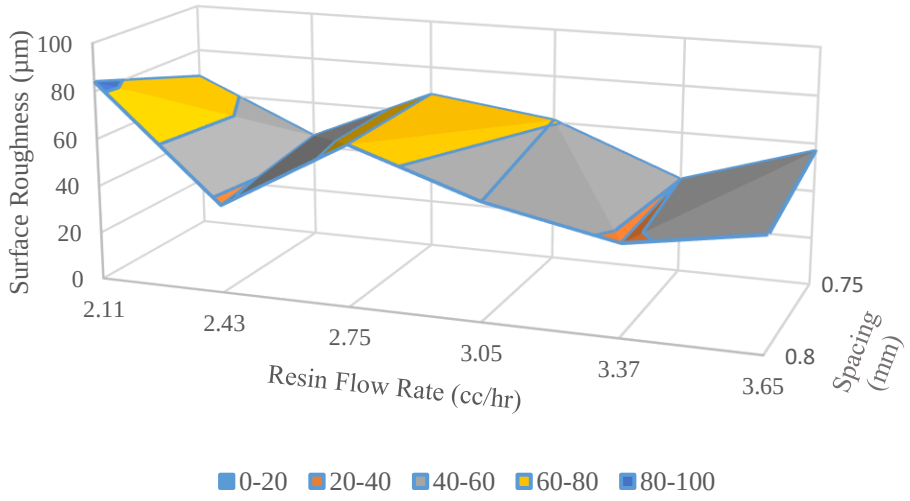

Figure 22: Surface roughness map of prints with 0.8 mm nozzle

In Figure 22, it can be noticed that in contrast to other nozzle sizes, only two spacing settings were tested for surface topography analysis. The reason behind this was that the reduction of spacing any lower than 0.75 mm resulted in constant failure during the print due to interference and the prepregs inability to make tight corners with such small radius.

8.2. Composition

V_f was one of the most important factors dictating the mechanical properties of 3D printed FRCs. Besides, the amount, size, and distribution of voids inside the prints also significantly influenced the mechanical behavior of the 3D printed composite materials. In different print

configurations, the CF tow count was kept constant at 1K, but depending on the spacing and nozzle size, the resin rate was varied. So, essentially, the percentage fiber content was varied by the setting up of different printing configurations. As discussed in an earlier section, burnoff tests were conducted to determine the V_f of composites that were 3D printed with varying configurations of printing. The results obtained from the burnoff test are presented in Figure 23.

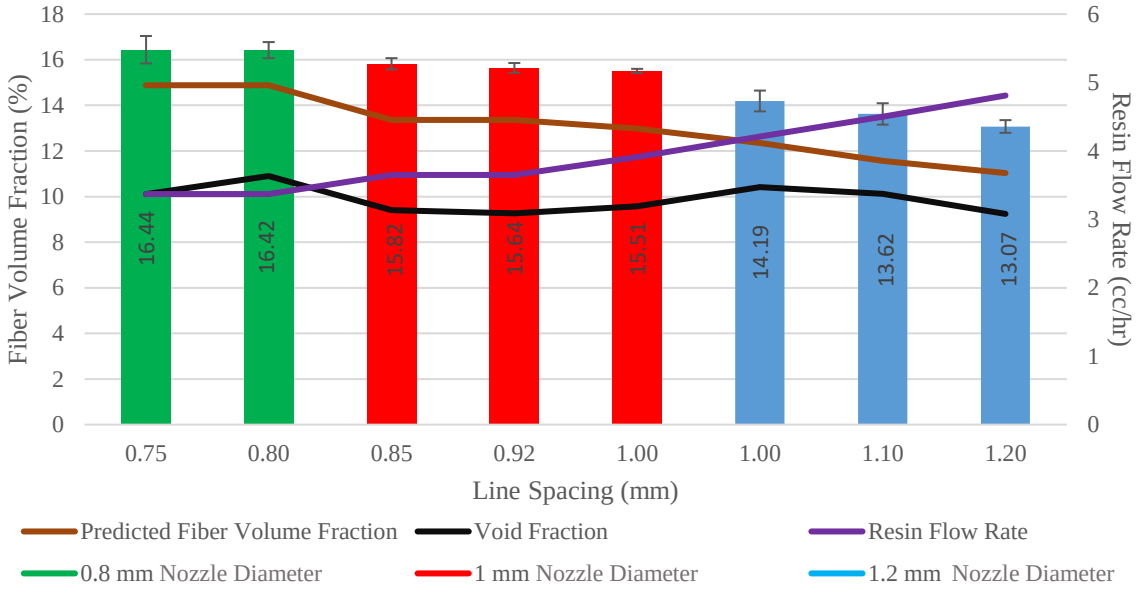

Figure 23: Composition of 3D printed composite resulting from different printing parameters

The variation of V_f data is statistically significant as the *P*-value in single factor ANOVA test was 3.4×10^{-47}. The burnoff test result showed V_f variation from 14.28% to 16.43%, depending on the nozzle and spacing configurations. These results show a significant improvement in V_f compared with the results reported (6-7% V_f) in a previous study that utilized a similar 3D printing mechanism [59]. Although these studies used CF with the same tow count (1k) and comparable resins, the twofold increase of V_f was achieved mainly via tighter packing of fiber tows. The current study set the layer thickness at 0.4 mm compared to 1 mm in previously reported studies [59].

Small standard deviations of V_f data indicated consistency of the printing variables and test procedures. Figure 23 also shows $\dot{V}_r$ values that were set for different configurations. The plot showed that the resin supply rate and the final V_f results are agreement with each other. For example, for 0.75 mm and 0.8 mm spacing with 0.8 mm nozzles, $\dot{V}_r$ was kept constant at 2.81 cc/hr. The V_f results of the specimens printed with these two configurations were almost equal. Again, for the 1.2 mm nozzles, $\dot{V}_r$ was incrementally changed with the increment of spacing. V_f of printed specimens from these configurations decreased in a similar trend with the increased $\dot{V}_r$. This trend of decreasing V_f was expected from the incremental $\dot{V}_r$.

With the assumption of no resin backflow through the fiber entry port, the final V_f of the 3D printed specimens could be theoretically calculated with a set value of $\dot{V}_r$. The fiber volume fraction of the prepreg V_{fp} was calculated to theoretically predict the V_f of printed specimens. For this, the mass of fiber tow with unit length was measured before and after the fiber to prepreg conversion process. From the difference between these two mass values, V_{fp} was calculated using Equation 8.2. Here, w_f and w_p are mass of fiber tow with unit length before and after prepreg conversion respectively. ρ_r and ρ_f are the density of resin (cured) and fiber tow, respectively. From this calculation, V_{fp} was found to be around 67%. After this, based on the printing parameters, V_f of final print was predicted using Equation 8.3.

$$V_{fp} = \frac{w_f/\rho_f}{(w_p - w_f)/\rho_r + w_f/\rho_f} \tag{8.2}$$

$$V_f = \frac{w_f/\rho_f}{(w_p - w_f)/\rho_r + w_f/\rho_f + \dot{V}_r/s} \tag{8.3}$$

The theoretically predicted values of V_f were plotted along with the actual V_f (from burnoff test) in Figure 23. This plot showed that the theoretically calculated V_f consistently underestimated

the actual fiber content found from burnoff test results. This discrepancy could result from the evaporation of thermal decomposition products during the curing of the polymer. Another reason behind the lower estimation of V_f could be a small amount of resin bleeding through the fiber inlet. However, the estimated V_f and results from burnoff results showed similar trends.

The void content also influenced the mechanical properties of the 3D printed composite specimens. Micro CT scanning of the 3D printed specimens was carried out to estimate the percentage of void contents. A sample Micro CT result (1.2 mm nozzle and 1.2 mm spacing) is shown in Figure 24. Micro CT results showed that 75% of the void sizes smaller than 0.000009 mm^3. The void fractions (V_v) from the Micro CT tests were also plotted in Figure 23. The results showed that V_v ranged between 9.24-10.9%. It is important to mention that the thermosetting resin, utilized in the study, had a volumetric shrinkage of 7% during the curing process [66]. Moreover, a 2.24% (volumetric) thermal initiator was mixed with the resin, which evaporated during the curing process. In total, the volume loss after curing was ~9.24% which was very close to the Micro CT reported void fraction. At this point, a relationship between the observed void fraction and hypothesized sources of the void is proposed by Equation 8.4. Here, V_s is the volumetric shrinkage rate of the UV curable thermoset resin. V_{ti} is the volumetric percentage of the decomposition products from thermal initiator, and V_{pr} is the void fraction introduced by improper print parameter setting and processing inefficiencies. According to this relation and the test data, 9.2% void fraction was from the formulation of the thermosetting resin system. The rest of the void (0.04-1.7%) could result from process imperfections. Further study is required to confirm this hypothesis.

$$V_v = V_s + V_{ti} + V_{pr} \tag{8.4}$$

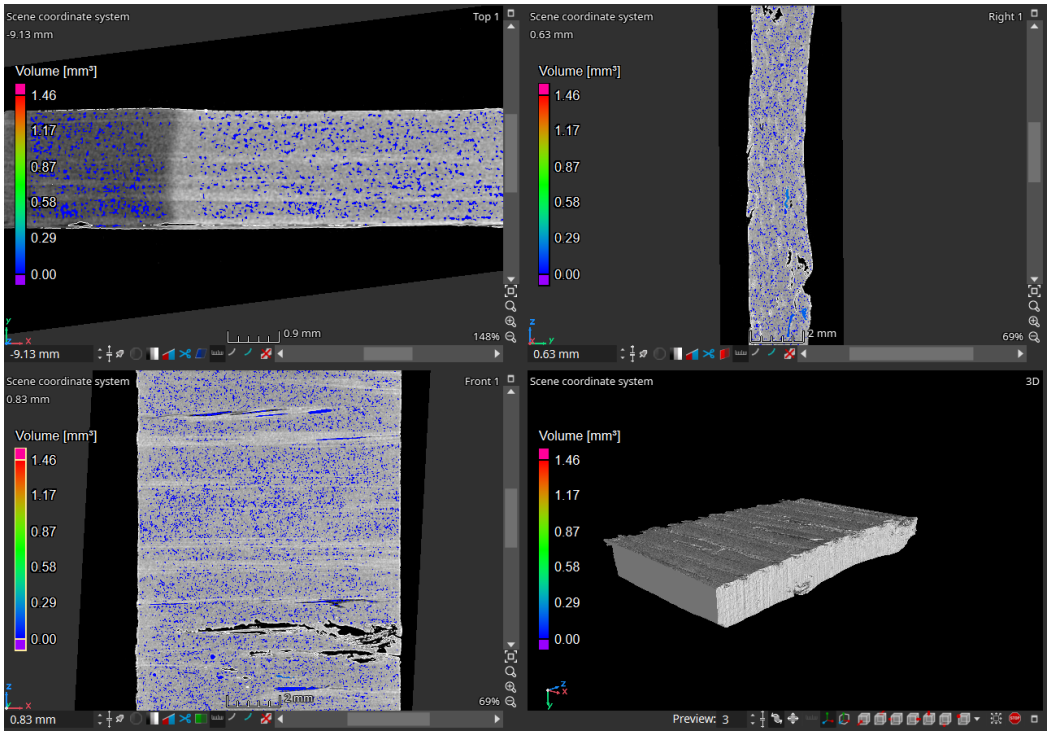

Figure 24: Micro CT of printed and post-cured specimen
Figure Note: This specific sample was printed using a 1.2 mm nozzle and 1.2 mm spacing

8.3. Tensile Properties

The behavior of the 3D printed composite specimens was tested under tensile loading up to failure. For each configuration of print parameters, 5 specimens were tested for tensile property determination. The average tensile strengths obtained from tensile tests are presented in Figure 25. In addition to experimentally obtaining the tensile properties, the tensile strength and modulus were theoretically calculated using the Rule of Mixtures (ROM). ROM for tensile strength and modulus are expressed by the Equations 8.5 & 8.6, respectively. In these equations σ_{cu}, σ_{fu} and σ_{mu} are ultimate strengths of composite, fiber, and matrix, respectively. Here, E_c, E_f, and E_m are tensile elastic moduli of composite, fiber, and matrix, respectively.

$$\sigma_{cu} = [\sigma_{fu}V_f + \sigma_{mu}(1 - V_f)]\,(1 - V_v) \tag{8.5}$$

$$E_c = [E_f V_f + E_m(1 - V_f)](1 - V_v) \tag{8.6}$$

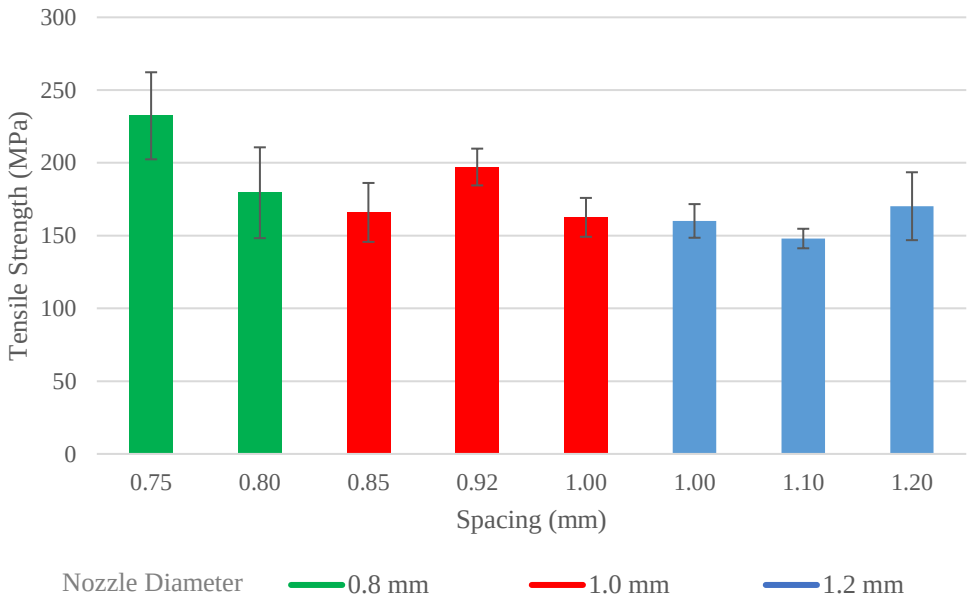

Figure 25: Tensile strength of 3D printed specimens

Statistical significance in the change of average tensile strength was observed as *P*-value of tensile strength data was 0.000122 from one-way ANOVA test. From the data presented in Figure 25, a general trend of increasing tensile strength with the decreased resin flow rate can be observed. The specimens with the lowest spacing between the printed lines (0.75 mm) demonstrated the maximum average ultimate tensile strength of 232.35 MPa. According to the rule of mixture (ROM), the tensile strength should increase with increasing V_f of unidirectional FRC. A comparison of data points from Figure 25 showed that the nozzle diameter and spacing directly influenced both the V_f and tensile properties of the composites. Two different spacing configurations (0.8 mm and 0.75 mm) were used for printing with 0.8 mm nozzles. As $\dot{V}_r$ was the same for these two settings, V_fs of the printed composites was also almost equal. But comparing the results shown in Figure 24, it was observed that the tensile strengths of the specimens with these two settings were significantly different. The amount of fiber and resin delivered to the print was the same for these two configurations, but printing with closer line spacing produced

specimens with smaller cross-sectional areas. So, though the tensile loads carried by these two types of specimens were similar, the specimens with less line spacing had higher tensile strength. While keeping the $\dot{V}_r$ constant, increasing the spacing also increased the void content in the composite. This increase in void contents was observed in the plot in Figure 23. As a result, the high void content in the specimens printed with 0.8 mm nozzle and 0.8 mm spacing reduced the ultimate tensile strength sustained by the composite specimens.

As the CF tow count was fixed, printing with a smaller diameter nozzle and tighter spacing required less resin in the matrix, which resulted in higher V_f. So, according to the ROM, printing with a smaller diameter nozzle and a closer spacing should produce specimens with greater tensile strength. That trend was observed in the results from 3 different nozzle sizes. The maximum tensile strength achieved by the specimens printed with varying nozzle sizes increased with decrease of nozzle diameter. However, the relationship between tensile strength and spacing is slightly different according to the test results. Among the specimens printed with 1.2 mm nozzles, maximum tensile strength was exhibited by the specimens printed with 1.2 mm spacing (max spacing). For 1.0 mm and 0.8 mm diameter nozzles, line spacing for max tensile strength was 0.92 mm and 0.75 mm, respectively. The void content in the composites might have played a significant role in determining the strength of composites printed with different line spacing. For example, specimens printed with 1.1 mm spacing had a greater V_f compared to the specimens printed with 1.2 mm spacing. So, according to ROM, specimens printed with 1.1 mm spacing should be stronger than specimens printed with 1.2 mm spacing. But the tensile test data in Figure 25 showed the opposite situation. It should be considered that the void volume fraction (V_v) was slightly lower in the specimens printed with 1.2 mm spacing, which resulted in producing stronger specimens under tensile loading. The effect of void content is further discussed in later sections.

The tensile strength of the 3D printed composites was predicted using the ROM calculations. A plot comparing the theoretical (from ROM calculations) and experimental tensile strength is presented in Figure 26. This plot shows that the strength values obtained from tensile test ranged between 30-45% of ROM predicted strength values. The fluctuation of the ratio of experimental to theoretical tensile strengths (strength ratio) could be a result of multiple factors, such as void fraction V_v, void distribution, and statistical errors. Larger sample number could narrow down the statistical variability. However, a comparison of the strength ratio within the results obtained from a fixed nozzle size indicates that the strength ratio is sensitive to void fractions. A probable cause for this sensitivity of strength ratio is the void distribution. The ROM prediction of tensile strength factored in the total void volume, but the concentration of void contents in close vicinity could further adversely affect the actual tensile strength. Increased amount of void content increased the probability of local concentration of voids. Thus, the actual tensile strength dropped significantly with a slight increment of V_v, compared to ROM predicted values. A definitive statement about the exact mechanism and effect void on the tensile strength of 3D printed unidirectional FRCs requires further in-depth studies.

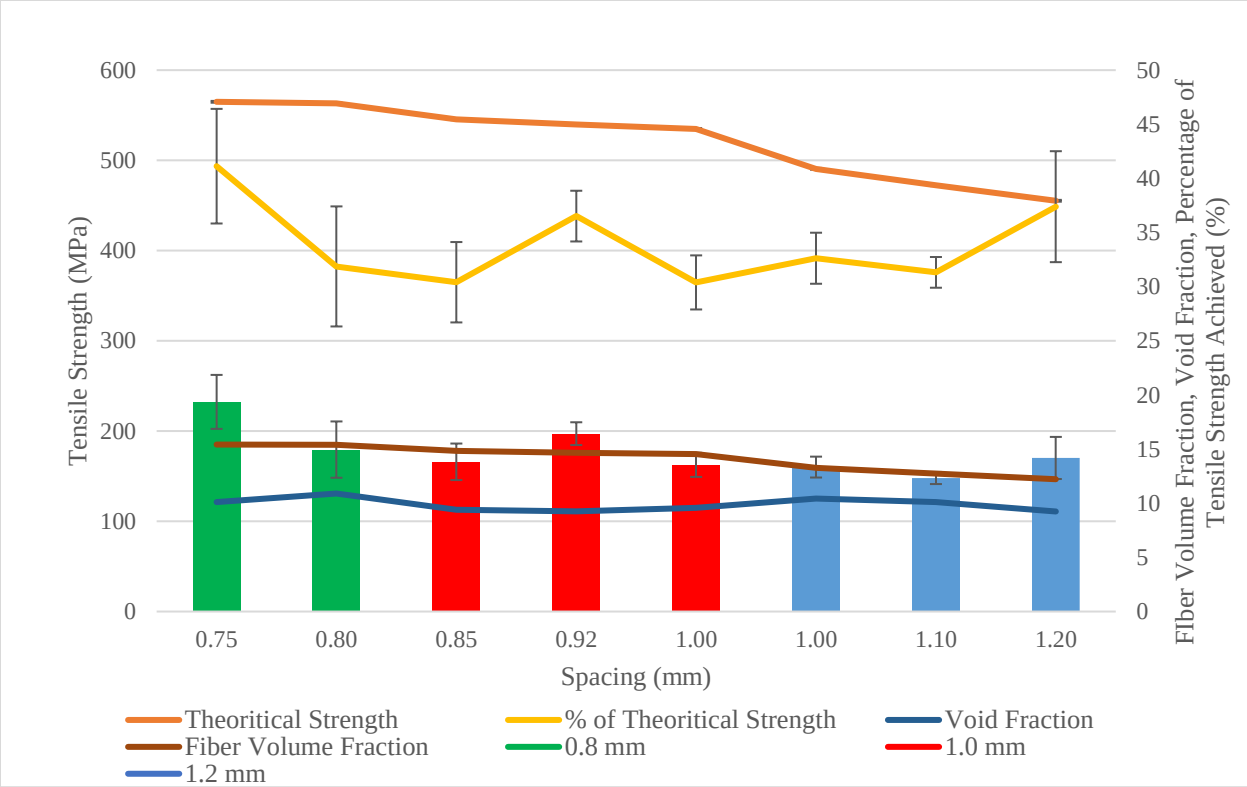

Figure 26: Theoretical and experimental tensile strength

Modulus of Elasticity of the 3D printed specimens exhibited a significant difference between experimental results and expected values from ROM. The comparison is presented in Figure 27. The experimental tensile modulus varied between 68-81% of the ROM predicted values. The ROM model assumed that the unidirectional filaments were perfectly straight. But, in practice, the microscopic images revealed slight waviness of the CF filaments in the printed lines. Hsiao *et al.* [67] showed that the waviness in the reinforcing filaments in unidirectional FRC could dramatically reduce the tensile modulus of the composite. Based on this, it can be argued that waviness could be a major contributor to the discrepancy between the tensile modulus's theoretical and experimental values. Some of the waviness of filaments originated from the twist in the CF tow. A good portion of the waviness could be attributed to the prepreg feeding technique. During the 3D printing of the current study, a slack at prepreg (located between the spool and nozzle) was

maintained all the time. This was done to reduce the drag experienced by prepreg while going through the right-angle turn at the nozzle outlet tip. The friction generated at this turn could damage and snap the prepreg at the outlet tip. In a previous study [59] similar prepreg feeding mechanism was utilized, except that the prepreg was unspooled by the tension generated from the print. The self-unspooling mechanism allowed CF prepreg to be laid in a less wavy fashion. That study reported almost equal experimental and theoretical tensile modulus of 3D printed unidirectional FRCs. These results support the argument that the filament waviness caused the theoretical vs. experimental tensile moduli discrepancy.

Another potential cause for the discrepancy between the theoretical and experimental values of tensile moduli could be insufficient interfacial bonding between fiber filaments and the matrix. As mentioned in earlier sections, the CF surface sizing was manipulated to bond with epoxy matrix. As this study used urethane polymer matrix, this could be a potential reason for experimental tensile moduli to be less than the theoretical ones.

The maximum average tensile modulus was 31.19 GPa. This is 1.5 times the previously reported tensile modulus with a similar 3D printing technique[59]. It is worth mentioning that the fluctuation of experimental tensile moduli exhibits a similar trend of experimental ultimate tensile strength fluctuation. So, the void fraction might have had a role in the variation of tensile modulus as well. Nevertheless, the sensitivity of modulus to the void fraction was not as profound as it was for the ultimate tensile stress. The tensile modulus of these printed composites has room for improvement, when compared with the ROM predicted values.

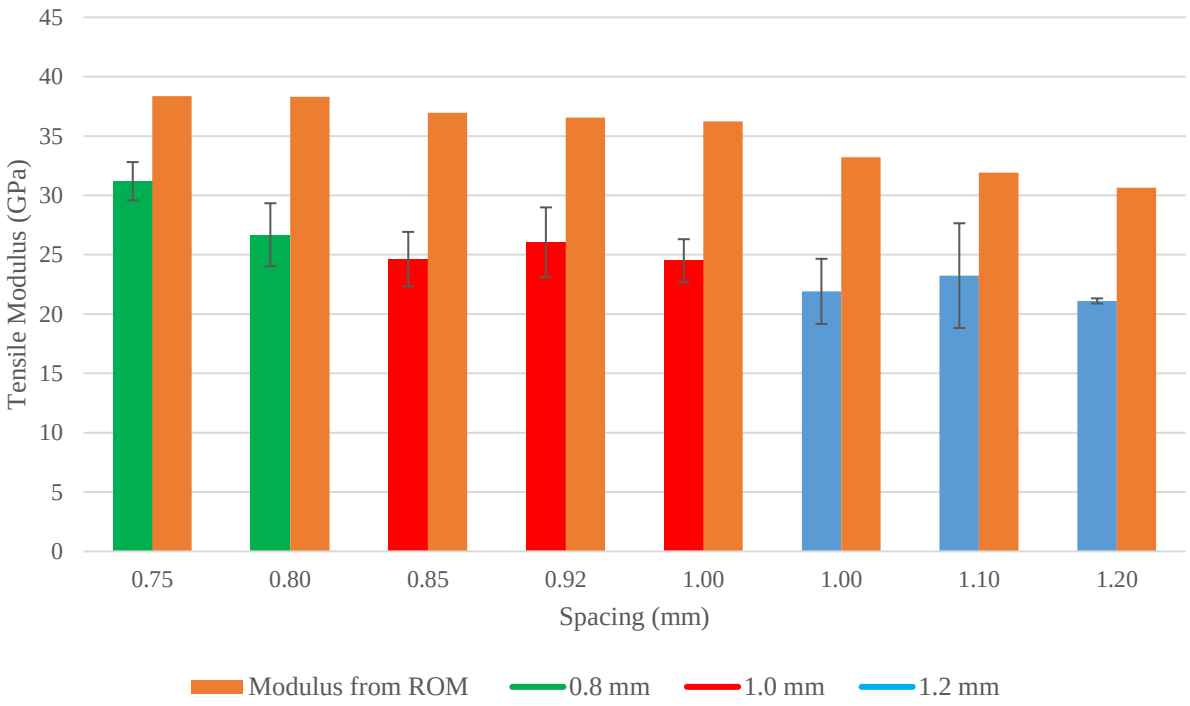

Figure 27: Tensile modulus

While tensile strengths and tensile moduli showed a distinct trend of higher values for specimens with tightly packed prepreg tow, the tensile strains did not show any distinct trend with the variation of nozzle size, spacing, or resin flow rate. Figure 28 shows the average ultimate tensile strains of specimens printed with different printer configurations. Although the average ultimate tensile strain fluctuation had a pattern similar to the pattern of strength fluctuations, the overall strain data does not show any increasing or decreasing trend over the parameter change. One-way ANOVA of the ultimate tensile strain data calculated a *P*-value of 0.0493. So, the null hypothesis that the mean values of strain at failure were the same for different groups could be rejected. Nevertheless, the regressive linear trendline was almost horizontal in Figure 28, meaning no changing trend of ultimate tensile strain values for prints with different print parameters. It is also worth mentioning that the ultimate tensile strains for all specimens are lower than the individual ultimate strains of both fiber and matrix. From the ultimate strain results, it was

suspected that the interfacial failure could influence the of these composite bars' overall failure mechanism. The insufficient interfacial bonding could also be the reason behind the 30-40% strength achieved by the composites when compared against the ROM predicted strength values. It is a plausible explanation as the resin used in this study was Urethane based and, the CF filaments had sizing designed to bond with epoxies. The mismatch of sizing and of filaments and the resin, used in this study, could be a probable cause for interfacial slip and failure. It is also possible that the range of V_f , studied in this project, was not wide enough to view the effect of V_f on the ultimate tensile strain endured by the 3D printed unidirectional FRCs.

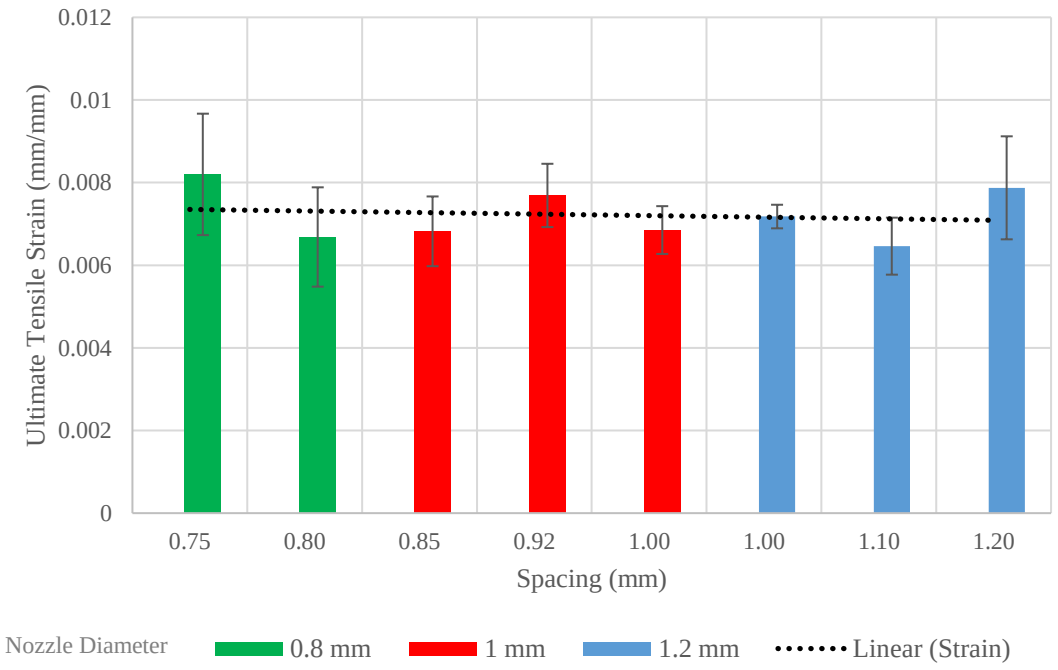

Figure 28: Ultimate tensile strain of 3D printed specimens

A sample stress-strain curve (configured as nozzle diameter =1.2 mm and spacing =1.2 mm) is presented in Figure 29. All 3D printed specimens, in this study, exhibited similar stress-strain behavior. The stress-strain plots suggested brittle failure of the 3D printed composite specimen. These plots were linear until rupture. The tensile stress-strain curves showed no yielding

before the rupture of specimens, thus indicating brittle type failure of the composite. The failure surfaces were perpendicular to the length of the specimen, which further supported brittle type failure of the specimens. The small slip in the plot may have originated from micro-failure in interlaminar region.

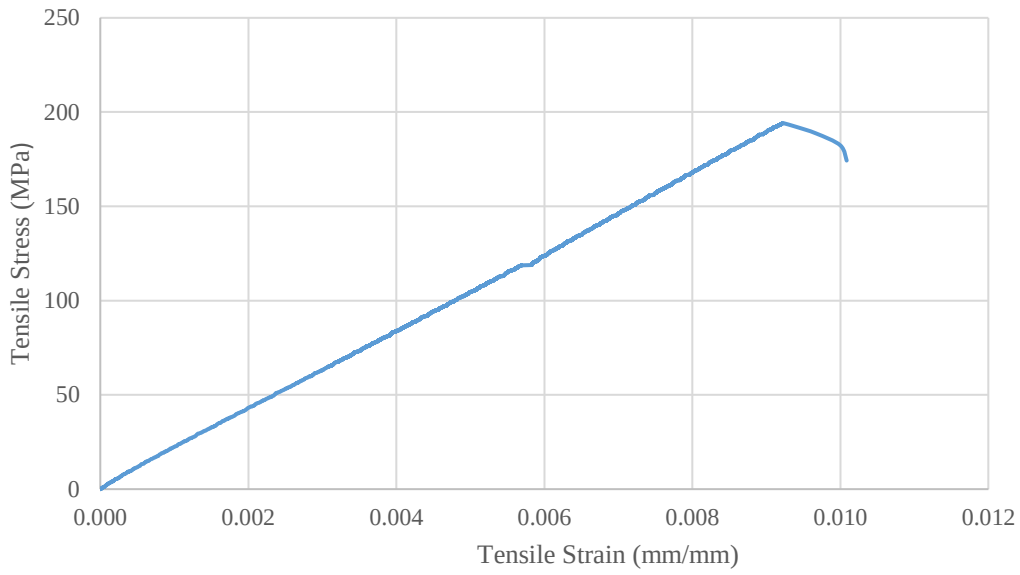

Figure 29: Stress- strain curve under tensile loading

The tensile properties of the specimens printed in this study was compared with the tensile properties of the specimens printed by Markforged continuous fiber reinforced composite printer (Markforged, Mark II, Watertown, MA, USA). The printed composites in this study exhibited slightly higher strength and failure strains compared to the composites printed with Markforged (Strength=221 MPa, Ultimate strain=0.066 mm/mm, Tensile modulus=3.31 GPa) [68]. A very significant improvement with the printing process in this study over Markforged is the tensile modulus. The printed composites exhibited 10 times higher tensile modulus compared to Markforged printed composites. The higher modulus of the studied composites originated from the selection of thermoset resin instead of thermoplastics. Layer thickness and number of layers are two key factors in this comparison. The Markforged printed composites were characterized

using prints with 16 layers (layer thickness= 0.125 mm) where is the current study characterized prints with 6 layers (layer thickness 0.4mm). Further reduction in layer thickness, in current study, could yield prints with higher properties.

8.4. Flexural Properties

Flexural strength, modulus and the ultimate flexural strain of the 3D printed FRCs were tested through the 3-point bending test. The flexural stress strain curve of a specimen printed with a 1.0 mm nozzle and 1.0 mm spacing is shown in Figure 30. All 3D printed composite specimens tested in this study exhibited similar flexural behavior. The flexural strain plot against the applied flexural stress was slightly curved for all test specimens. This nonlinearity for unidirectional CF reinforced composites had been reported in the literature. Sideridis *et al.* [69] showed that a compressive failure zone underneath the loading nose preceded flexural failure. This compressive failure zone contributed to the nonlinearity of the flexural stress strain curve. He *et al.* [70] did flexural studies of unidirectional CF composites and explained their flexural responses with different failure modes. The study experimented with crack initiation and propagation methods in the matrix phase depending on the flexural load level and fiber volume fraction. The deformation and micro cracking of the matrix material at higher flexural loads resulted in a decrease in overall composite flexural modulus, thus generating a nonlinearity of stress-strain behavior. This explanation of the nonlinearity of flexural stress-strain curves was also supported by the inspection of failure surfaces of the 3D printed composites under 3-point bending tests. It was observed that the matrix material failed on a horizontal surface at the neutral axis of flexural deformation. This suggested that interlaminar sliding took place prior to the flexural failure.

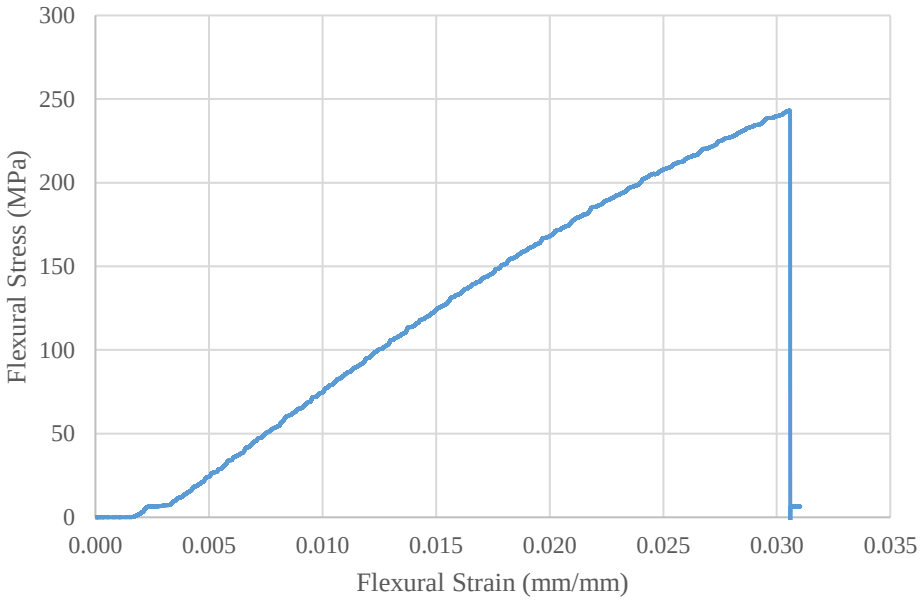

Figure 30: Flexural stress-strain curve

Flexural strength results of printed composites were plotted in Figure 31. This plot revealed that the change in flexural strength followed almost the same trend as the change of V_f. Deviation from this trend (prints with 0.8 mm nozzle and 0.8 mm spacing) could be correlated to increased void content in the printed specimens. Specimens printed with the smallest line spacing exhibited the maximum average flexural strength of 373 MPa. Though V_f was the same for the two spacing settings for 0.8 mm nozzles, the flexural strength of the prints with 0.8 mm line spacing was significantly lower than that of 0.75 mm line spacing. This reduction in flexural strength can be correlated to the increased V_v of the prints with 0.75 mm spacing. However, compared to tensile and flexural results, the flexural strength showed a better match with the V_f trend. This suggested that the flexural strength is comparatively less susceptible to the void fraction. This effect was probably observed since flexural failure takes place under the loading nose of the three-point bending test. Thus, it is less likely to be affected by a localized conglomeration of voids.

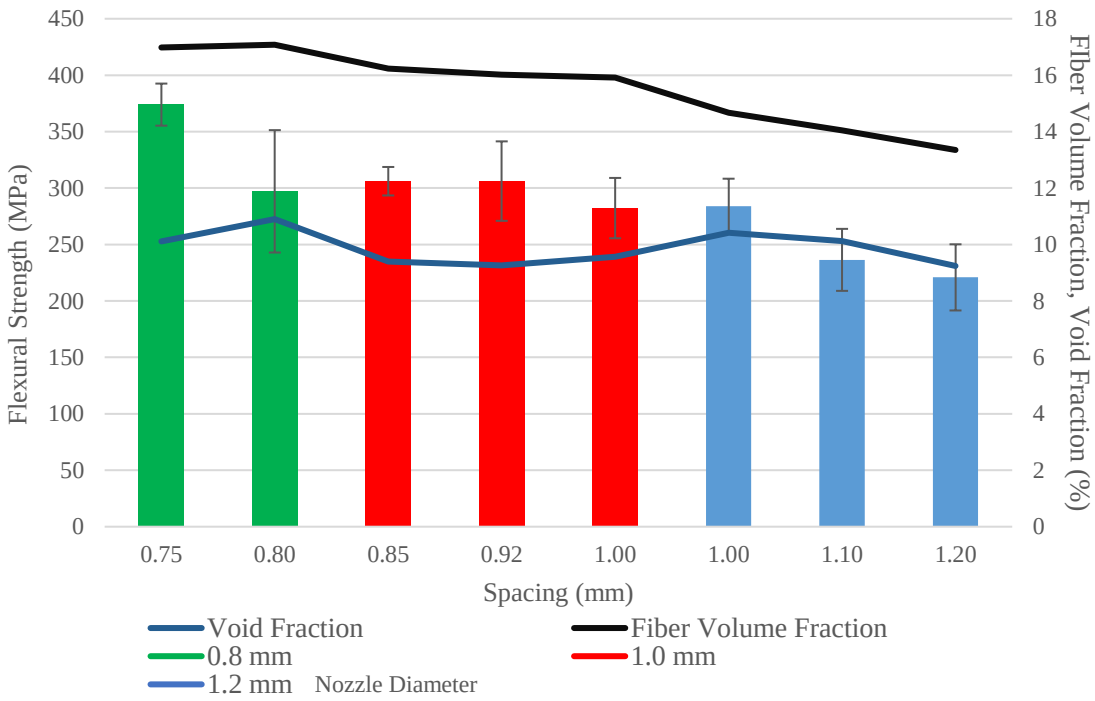

Figure 31: Flexural strength of 3D printed composites

Figure 32 shows the plot of flexural modulus exhibited by printed composites. Unlike the tensile modulus, the flexural modulus showed a more consistent effect from the line spacing settings. This effect could be due to the nature of fiber and matrix material distribution. This is an interesting observation and warrants further study. The trend in change of flexural strength was statistically significant as *P*-value was found calculated to be 1.07×10^{-5}.

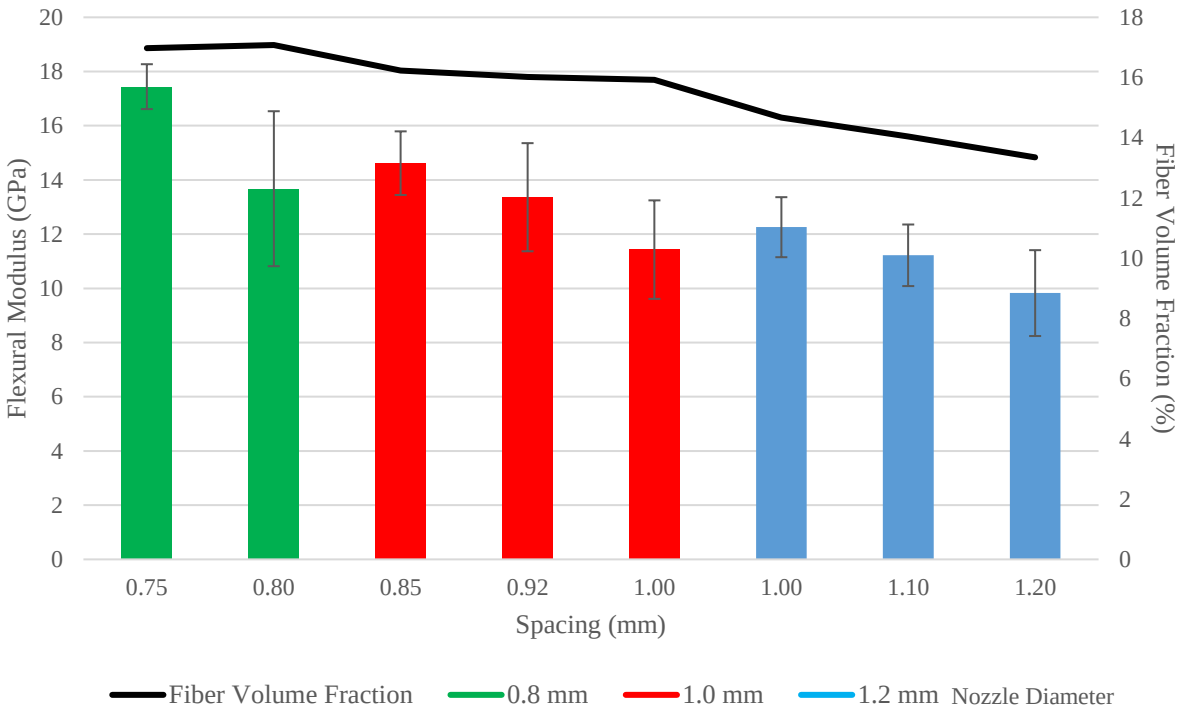

Figure 32: Flexural modulus of 3D printed composites

The plot of ultimate flexural strains is shown in Figure 33. Like the tensile strains at failure, flexural strains at failure also did not show any increasing or decreasing trend over the print parameter changes. ANOVA test *P*-value for the sample data was significantly smaller than 0.05; thus, the mean ultimate flexural strain variation for 3D printed specimens was statistically significant. Nevertheless, no trend in change of ultimate flexural strain was observed from the plot.

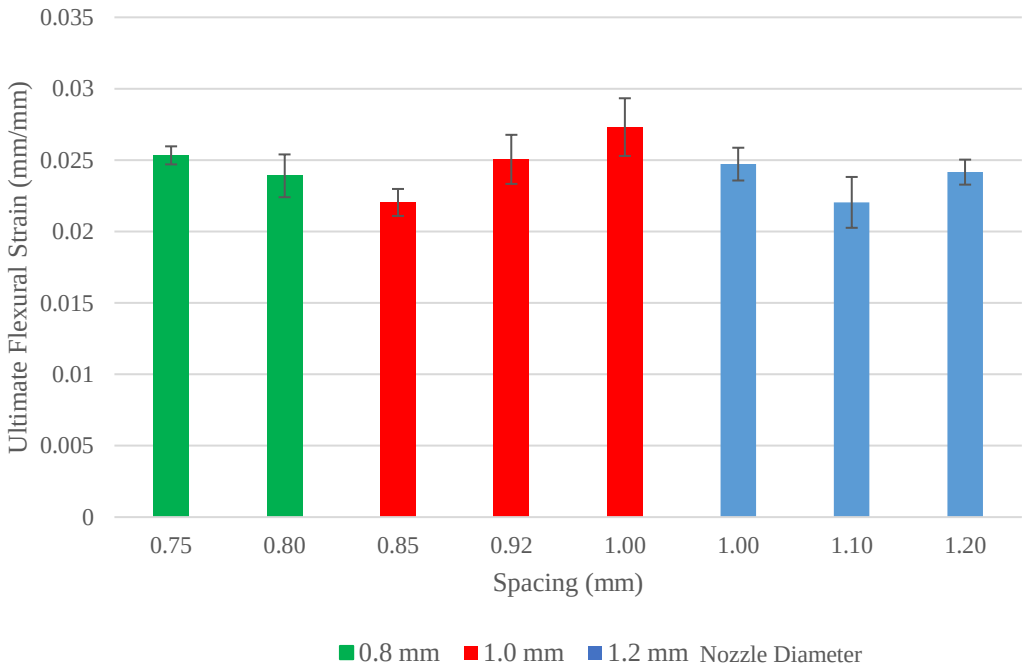

Figure 33: Ultimate flexural strain of 3D printed composites

8.5. Thermal Stability

TGA tests were conducted on the printed composites o obtain the onset of degradation temperature. The specimens with the highest and lowest configurations were chosen for TGA analysis. TGA tests were done within 25 to 600 ºC with a ramp rate of 20 ºC/min. TGA curves of all the specimens were almost identical and showed no significant change in the onset point of degradation temperature. A sample of the TGA analysis curve is presented in Figure 34. The average degradation temperature was 382 ºC. V_f was also calculated from TGA results. The residual mass after TGA test were the fibers. For 0.8 mm nozzle and 0.75 mm spacing V_f from TGA was 17.31%. For 1.2 mm nozzle and 1.2 mm spacing V_f from TGA was 13.22%. These results were very close to the V_f calculated from burnoff tests. This validated the integrity of TGA and burnoff test data.

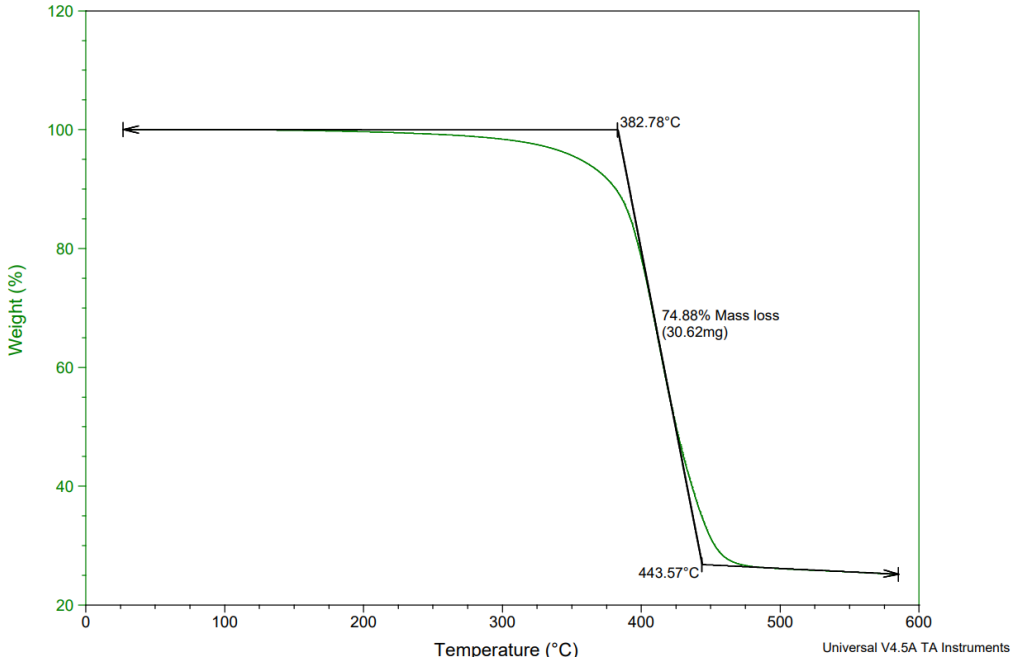

Figure 34: TGA analysis of 3D printed composite

DMA tests were conducted on three sets 3D printed specimens (0.8 mm, 1.0 mm, and 1.2 mm spacing). A sample DMA result is shown in Figure 35. The glass transition temperature (T_g) was measured at the point of $\tan\partial$ curve from DMA tests.

T_g values obtained from composite specimens printed with different print parameters are plotted in Figure 36. The variation of T_g values was analyzed with one-factor ANOVA tests. The *P*-value of ANOVA for the T_g was calculated to be 0.00315. So, the fluctuation of T_g for different print configurations was statistically significant. From Figure 36 a decreasing shift of T_g was observed with the decrease of V_f. The storage and loss modulus of the composites were tested at different temperatures with the DMA tests. It showed that at 1 Hz loading frequency, the damping effect of the composites were higher for prints done in larger spacings configurations.

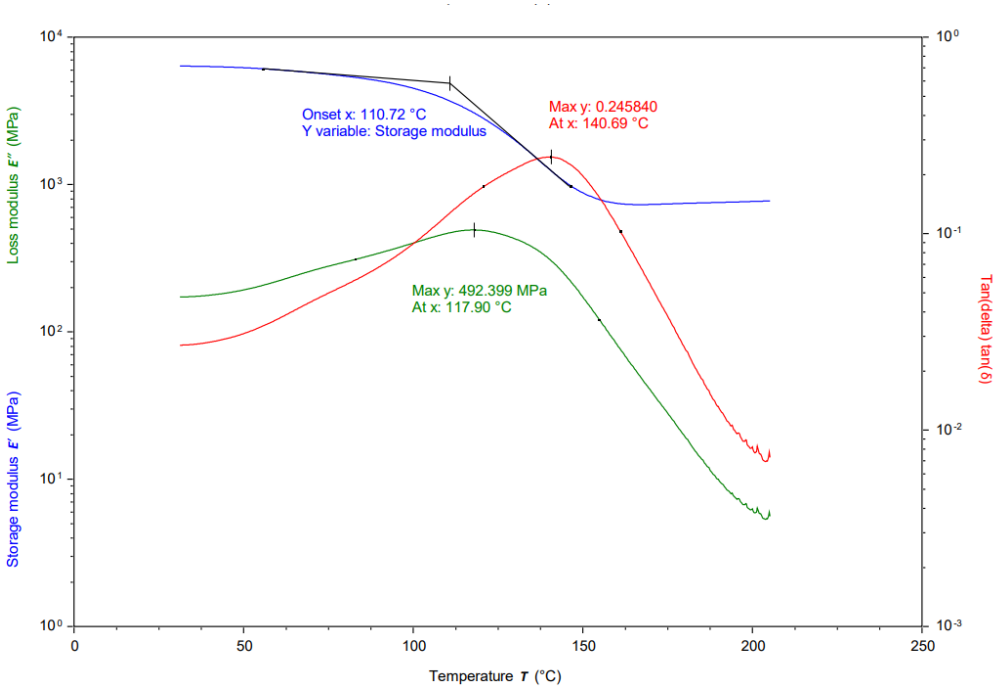

Figure 35: Sample results from DMA test of 3D printed composite specimen

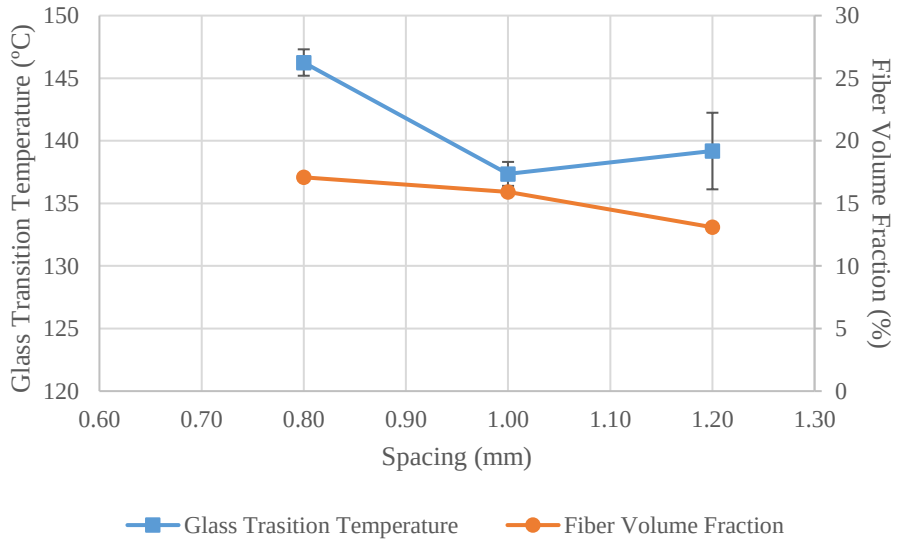

Figure 36: Glass transition temperature of 3D printed composite

9. CONCLUSION

A 3D printer, capable of printing with continuous fiber reinforced thermoset composite, was constructed. Development of control code with unique purpose of handling of continuous fiber reinforcement facilitated numerous adjustments of the process parameters. The thermoset resin was formulated with two stage curing functionality- UV and thermal curing. The multi-mode curing functionality allowed the resin system to be fully cured in the regions where UV could not penetrate. The formulation of CF prepreg ensured complete wetting of CF tow with the thermoset resin. This process also made the CF tow resilient to fraying at the printing nozzle tip.

Custom designed dispensing nozzle was used for encapsulating the CF prepreg with liquid UV and thermal curable resin system and dispense the composite into the print. Different nozzle diameters were experimented with as one of the control parameters of the composite 3D printing process. Topographic analysis of the printed surface showed that both resin flow rate and the spacing between the printed lines was needed to be adjusted for good quality 3D printed composites. With the help of surface roughness measurements obtained from the topographic analysis, certain configurations of nozzle sizes, resin flow rates and line spacings were identified. These configurations of parameters 3D printed composites with average surface roughness lower than 60 μm. Minimum line spacing of 0.75 mm was achieved for composite 3D printing with 1K CF tow.

The composition of the 3D printed composites were determined by burnoff and Micro CT tests. The change of the composition of the printed composite with the change of printing parameters was investigated. Maximum fiber volume fraction was achieved at 16.5%. The void content volume for specimens printed all configurations were found around 10%. Despite little fluctuations, the void fraction was stable for all the printing parameters configurations which

indicated satisfactory optimization of material dispensing process. It was hypothesized that significant portion of the void contents originated from the thermoset resin formulation. Further experimentation with different resin system could reduce the amount of void in the 3D printed composites.

Investigation of mechanical properties showed that both tensile and flexural properties of the printed composites can be improved by fine-tuning the print parameters. Maximum strength and modulus were exhibited by the specimens printed with the closest packing of fiber tows. However, specimens printed with 1 mm nozzle with 0.85-1.00 mm spacing zone showed least fluctuations around a fair level of strength. The number of print failure was low and the turning radius of fiber tow at the corners were also much consistent while 1 mm nozzle size was used for printing. So, this study recommends that for consistent composite 3D printing 1 mm nozzle with 0.92 mm spacing should be adopted. 0.75 mm spacing with 0.8 mm nozzle size can be used for achieving maximum mechanical properties. For 1.2 mm nozzles the recommended spacing for printing was 1.0 mm.

The study found that performance of 3D printed continuous fiber reinforced thermoset composite could be immensely enhanced by parameter optimization. The observations also suggested that there is great scope of enhancing the performance by optimization of material selection and formulation. The 3D printer that was constructed for this project was designed to be adaptive of using different types of fibers and UV curable resin systems. This study recommends further study with different materials with this 3D printing technique for further improvement of print performance.

10. RECOMMENDATIONS FOR FUTURE STUDIES

This study addressed the effect of a few process parameters on the performance of 3D printed continuous fiber-reinforced composites. The study showed that 3D printed FRCs could exhibit great mechanical strength and that the mechanical properties are subject to processing parameters. While conducting the experimental prints and testing, many aspects of these processes were observed, which require further study.

Due to processing restrictions, according to this study, the matrix volume fractions were above 80%. As matrix material occupied most space of the 3D printed composite, utilization of a thermoset resin system with enhanced mechanical properties can improve the mechanical properties of the final composites. This study utilized a urethane-based deft resin system. During the same time of this study, more resin systems were developed both in research studies and in the commercial market. Using the same process of this study, utilization of the latest and greatest resin systems is worth further studies.

Increasing the fiber volume fraction in the printed objects would also help enhance the mechanical properties. This study tried optimizing the printing process while utilizing 1K CF tow for achieving the finest resolutions. However, increasing the CF tow count to 3K or 6K could increase the fiber volume fractions, thus increasing the mechanical strength. Exploration with larger filament count fiber tows is suggested in future studies.

As mentioned in earlier sections, the improper match of filament surface sizing and matrix material could be a potential cause for the discrepancy in theoretical vs. experimental properties of the composites. Further studies are required to investigate filament surface chemistry's effect on the printed objects' final mechanical properties.

Another potential limiting factor of the mechanical properties of the printed objects is the presence of gaps and voids in the prints. As discussed earlier, some voids could have originated from the evaporation of the thermal initiator in the resin system. Further studies are required to study this factor and find a better-suited thermal initiator composition for the resin system. It was also discussed that the shrinkage of the resin upon total curing could also create gaps in the printed objects. Experimentation with resins with a lower shrinkage rate is required to support this hypothesis and further reduce the voids in the printed object.

It was observed that the 3D printer constructed based on the 3-axis movement of the printing nozzle had a limitation of prepreg handling. As the printing nozzle had to be placed in an upright orientation, the prepreg had to make a right-angle turn at the nozzle tip. This turn had a damaging effect on the prepreg, and to counteract that, the nozzle diameter had to be wider, thus hurting the fiber volume fractions. Based on this study's experimental learnings, a slated nozzle orientation with the print bed should be gentler on the prepreg while laying it into the print. To achieve this a 4-axis printing setup is recommended with one rotational movement capability around the Z-axis.

It was discussed in this study that the presence of gaps and flaws in the printed objects could also be a reason behind the lower tensile properties displayed during the testing. A continuous monitoring system that can detect defects while printing could be deployed and tested in future studies. During the current study, it was observed that the flaws could be identified by laser line profiles projected perpendicular to printed lines. An AI algorithm could be trained to detect those imperfections by real-time image processing and take corrective measures.

To conclude, depending on the findings of this study, it was learned that there were still a lot of aspects where further studies could immensely improve both the printing process and the properties of the printed objects.

REFERENCES

1. Wang, X., et al., *3D printing of polymer matrix composites: A review and prospective.* Composites Part B: Engineering, 2017. **110**: p. 442-458.
2. Levy, G.N., R. Schindel, and J.-P. Kruth, *Rapid manufacturing and rapid tooling with layer manufacturing (LM) technologies, state of the art and future perspectives.* CIRP annals, 2003. **52**(2): p. 589-609.
3. Horn, T.J. and O.L. Harrysson, *Overview of current additive manufacturing technologies and selected applications.* Science progress, 2012. **95**(3): p. 255-282.
4. Wong, K.V. and A. Hernandez, *A review of additive manufacturing.* International scholarly research notices, 2012. **2012**.
5. Su, A. and S.J. Al'Aref, *History of 3D printing*, in *3D Printing Applications in Cardiovascular Medicine*. 2018, Elsevier. p. 1-10.
6. Hull, C.W., *Apparatus for production of three-dimensional objects by stereolithography. US 4575330 A, Google Patents*. 1986.
7. Ligon, S.C., et al., *Polymers for 3D printing and customized additive manufacturing.* Chemical reviews, 2017. **117**(15): p. 10212-10290.
8. Wang, B., et al., *Current progress on the 3D printing of thermosets.* Advanced Composites and Hybrid Materials, 2020: p. 1-11.
9. Brooks, G., K. Kinsley, and T. Owens, *3D printing as a consumer technology business model.* International Journal of Management & Information Systems (IJMIS), 2014. **18**(4): p. 271-280.
10. Groth, C., et al., *Three-dimensional printing technology.* J Clin Orthod, 2014. **48**(8): p. 475-85.
11. Ngo, T.D., et al., *Additive manufacturing (3D printing): A review of materials, methods, applications and challenges.* Composites Part B: Engineering, 2018. **143**: p. 172-196.
12. Prajapati, H., et al., *Improved print quality in fused filament fabrication through localized dispensing of hot air around the deposited filament.* Additive Manufacturing, 2021. **40**: p. 101917.
13. Tappa, K. and U. Jammalamadaka, *Novel biomaterials used in medical 3D printing techniques.* Journal of functional biomaterials, 2018. **9**(1): p. 17.
14. Canizares, A., J. Pazos, and D. Benítez. *On the use of 3D printing technology towards the development of a low-cost robotic prosthetic arm*. IEEE.
15. Joshi, S.C. and A.A. Sheikh, *3D printing in aerospace and its long-term sustainability.* Virtual and Physical Prototyping, 2015. **10**(4): p. 175-185.
16. Bekas, D.G., et al., *3D printing to enable multifunctionality in polymer-based composites: A review.* Composites Part B: Engineering, 2019. **179**: p. 107540.
17. Singh, S., S. Ramakrishna, and F. Berto, *3D Printing of polymer composites: A short review.* Material Design & Processing Communications, 2020. **2**(2): p. e97.
18. Matsuzaki, R., et al., *Three-dimensional printing of continuous-fiber composites by in-nozzle impregnation.* Scientific reports, 2016. **6**(1): p. 1-7.
19. Borrello, J., et al., *3D printing a mechanically-tunable acrylate resin on a commercial DLP-SLA printer.* Additive manufacturing, 2018. **23**: p. 374-380.
20. Shukla, V., et al., *Review of basic chemistry of UV-curing technology.* Pigment & Resin Technology, 2004.

21. Endruweit, A., M.S. Johnson, and A.C. Long, *Curing of composite components by ultraviolet radiation: A review.* Polymer composites, 2006. **27**(2): p. 119-128.
22. Abliz, D., et al., *Curing methods for advanced polymer composites-a review.* Polymers and Polymer Composites, 2013. **21**(6): p. 341-348.
23. Mendes-Felipe, C., et al., *State-of-the-art and future challenges of UV curable polymer-based smart materials for printing technologies.* Advanced Materials Technologies, 2019. **4**(3): p. 1800618.
24. Wu, D., et al., *Mechanics of shape distortion of DLP 3D printed structures during UV post-curing.* Soft matter, 2019. **15**(30): p. 6151-6159.
25. Latouche, M. *hubs.com*. Available from: https://www.hubs.com/knowledge-base/sla-3d-printing-materials-compared/.
26. Sano, Y., et al., *3D printing of discontinuous and continuous fibre composites using stereolithography.* Additive Manufacturing, 2018. **24**: p. 521-527.
27. Wickramasinghe, S., T. Do, and P. Tran, *FDM-based 3D printing of polymer and associated composite: A review on mechanical properties, defects and treatments.* Polymers, 2020. **12**(7): p. 1529.
28. Carneiro, O.S., A.F. Silva, and R. Gomes, *Fused deposition modeling with polypropylene.* Materials & Design, 2015. **83**: p. 768-776.
29. Hu, Q., et al., *Manufacturing and 3D printing of continuous carbon fiber prepreg filament.* Journal of materials science, 2018. **53**(3): p. 1887-1898.
30. Ning, F., et al., *Additive manufacturing of carbon fiber reinforced thermoplastic composites using fused deposition modeling.* Composites Part B: Engineering, 2015. **80**: p. 369-378.
31. Shi, P. and J.C. Goh, *Self-assembled silk fibroin particles: Tunable size and appearance.* Powder technology, 2012. **215**: p. 85-90.
32. O'Connor, H.J. and D.P. Dowling, *Low-pressure additive manufacturing of continuous fiber-reinforced polymer composites.* Polymer Composites, 2019. **40**(11): p. 4329-4339.
33. Justo, J., et al., *Characterization of 3D printed long fibre reinforced composites.* Composite Structures, 2018. **185**: p. 537-548.
34. He, Q., et al., *3D printed continuous CF/PA6 composites: effect of microscopic voids on mechanical performance.* Composites Science and Technology, 2020. **191**: p. 108077.
35. Imeri, A., et al., *Fatigue analysis of the fiber reinforced additively manufactured objects.* The International Journal of Advanced Manufacturing Technology, 2018. **98**(9): p. 2717-2724.
36. Simpson, P.G., *Additive Manufacturing of Short-Fiber Composites via Stereolithography.* 2018.
37. Cheah, C.M., et al., *Mechanical characteristics of fiber-filled photo-polymer used in stereolithography.* Rapid Prototyping Journal, 1999. **5**(3): p. 112-119.
38. Lü, L., J. Fuh, and Y. Wong, *Improvements of mechanical properties by reinforcements*, in *Laser-Induced Materials and Processes for Rapid Prototyping*. 2001, Springer. p. 67-88.
39. Yunus, D.E., et al., *Short fiber reinforced 3d printed ceramic composite with shear induced alignment.* Ceramics International, 2017. **43**(15): p. 11766-11772.
40. Holthaus, M.J., *Short Glass Fiber Reinforced Composites Manufactured by Stereolithography*. 2021, North Dakota State University: Ann Arbor. p. 95.

41. Llewellyn-Jones, T.M., B.W. Drinkwater, and R.S. Trask, *3D printed components with ultrasonically arranged microscale structure.* Smart Materials and Structures, 2016. **25**(2): p. 02LT01.
42. *Fortify*. Available from: https://3dfortify.com/.
43. Struzziero, G., M. Barbezat, and A.A. Skordos, *Consolidation of continuous fibre reinforced composites in additive processes: A review.* Additive Manufacturing, 2021. **48**: p. 102458.
44. Wang, B., et al., *Fabrication of continuous carbon fiber mesh for lightning protection of large-scale wind-turbine blade by electron beam cured printing.* Additive Manufacturing, 2020. **31**: p. 100967.
45. Duan, Y., et al., *Effects of compaction and UV exposure on performance of acrylate/glass-fiber composites cured layer by layer.* Journal of Applied Polymer Science, 2012. **123**(6): p. 3799-3805.
46. Ming, Y., et al., *A novel route to fabricate high-performance 3D printed continuous fiber-reinforced thermosetting polymer composites.* Materials, 2019. **12**(9): p. 1369.
47. Ming, Y., et al., *Investigation on process parameters of 3D printed continuous carbon fiber-reinforced thermosetting epoxy composites.* Additive Manufacturing, 2020. **33**: p. 101184.
48. Xiao, H., et al., *A sensitivity analysis-based parameter optimization framework for 3D printing of continuous carbon fiber/epoxy composites.* Materials, 2019. **12**(23): p. 3961.
49. Mueller, J., et al., *Mechanical properties of interfaces in inkjet 3D printed single-and multi-material parts.* 3D Printing and Additive Manufacturing, 2017. **4**(4): p. 193-199.
50. Chou, D.-T., et al., *Novel processing of iron–manganese alloy-based biomaterials by inkjet 3-D printing.* Acta Biomaterialia, 2013. **9**(10): p. 8593-8603.
51. Compton, B.G. and J.A. Lewis, *3D-printing of lightweight cellular composites.* Advanced materials, 2014. **26**(34): p. 5930-5935.
52. Mueller, J., K. Shea, and C. Daraio, *Mechanical properties of parts fabricated with inkjet 3D printing through efficient experimental design.* Materials & Design, 2015. **86**: p. 902-912.
53. Hao, W., et al., *Preparation and characterization of 3D printed continuous carbon fiber reinforced thermosetting composites.* Polymer Testing, 2018. **65**: p. 29-34.
54. Shi, B., et al., *Dynamic capillary-driven additive manufacturing of continuous carbon fiber composite.* Matter, 2020. **2**(6): p. 1594-1604.
55. Ranabhat, B., S. Kirmse, and K.-T. Hsiao. *Feasibility study of novel magnetic compaction force assisted additive manufacturing (MCFA-AM) methodology for continuous carbon fiber reinforced polymer (C-CFRP) composites*.
56. Adumitroaie, A., et al., *Novel continuous fiber bi-matrix composite 3-D printing technology.* Materials, 2019. **12**(18): p. 3011.
57. He, X., et al., *3D printing of continuous fiber-reinforced thermoset composites.* Additive Manufacturing, 2021. **40**: p. 101921.
58. *Continuous Composites*. Available from: https://www.continuouscomposites.com/.
59. Rahman, M.A., et al., *3D printing of continuous carbon fiber reinforced thermoset composites using UV curable resin.* Polymer Composites, 2021.
60. *Peopoly*. Available from: https://peopoly.net/products/deft-resin-by-peopoly.
61. *Toray T300 Datasheet*. Available from: https://www.rockwestcomposites.com/media/wysiwyg/T300DataSheet_1.pdf.

62. ASTM, I., *D3039/D3039M-17 Standard Test Method for Tensile Properties of Polymer Matrix Composite Materials*. 2017, ASTM international: West Conshohocken, PA.
63. ASTM, I., *D7264/D7264M-21 Standard Test Method for Flexural Properties of Polymer Matrix Composite Materials*. 2021, ASTM International: West Conshohocken, PA.
64. ASTM, *ASTM D7028-07(2015)*, in *Standard Test Method for Glass Transition Temperature (DMA Tg) of Polymer Matrix Composites by Dynamic Mechanical Analysis (DMA)*. 2015, ASTM International: West Conshohocken, PA.
65. ASTM, I., *D3171-15 Standard Test Methods for Constituent Content of Composite Materials* . 2015: West Conshohocken, PA.
66. *Peopoly Deft resin shrinkage*. Available from: https://forum.peopoly.net/t/deft-resin-shrinkage/4798.
67. Hsiao, H.M. and I.M. Daniel, *Elastic properties of composites with fiber waviness.* Composites Part A: Applied Science and Manufacturing, 1996. **27**(10): p. 931-941.
68. Morgan, R.V., et al., *Markforged Continuous Fiber Composite Material Testing*. 2020, Los Alamos National Lab.(LANL), Los Alamos, NM (United States); New Mexico ….
69. Sideridis, E. and G.A. Papadopoulos, *Short-beam and three-point-bending tests for the study of shear and flexural properties in unidirectional-fiber-reinforced epoxy composites.* Journal of Applied Polymer Science, 2004. **93**(1): p. 63-74.
70. He, H.-w. and F. Gao, *Effect of fiber volume fraction on the flexural properties of unidirectional carbon fiber/epoxy composites.* International Journal of Polymer Analysis and Characterization, 2015. **20**(2): p. 180-189.

APPENDIX A. MECHANICAL CHARACTERIZATION TEST RESULTS

Table A 1: Tensile test results of specimens

Nozzle Diameter (mm)	Spacing (mm)	Sample Number	Tensile Strength (MPa)	Tensile Modulus (MPa)	Ultimate Tensile Strain (mm/mm)
0.80	0.75	1	183.811	32798	0.005913
		2	231.73	28585	0.008245
		3	259.24	32183	0.008834
		4	254.61	31216	0.010178
	0.80	1	236.89	29193	0.008834
		2	186.97	25161	0.01979
		3	165.66	28789	0.005497
		4	150.72	22185	0.016337
		5	157.09	28071	0.023989
1.00	0.85	1	180.16	25412	0.008274
		2	125.94	22002	0.005469
		3	171.566	26894	0.006361
		4	173.36	21806	0.007562
		5	178.68	27023	0.006907
	0.92	1	188.90	24342	0.00806
		2	203.75	26072	0.010547
		3	202.65	21618	0.014107
		4	213.21	30153	0.007279
		5	177.17	28027	0.008111
	1.00	1	173.52	23035	0.007948
		2	150.81	21909	0.011637
		3	168.37	25235	0.008531
		4	177.16	25332	0.008811
		5	142.90	26993	0.006405
1.2	1.00	1	182.79	26038	0.007025
		2	151.99	20184	0.007274
		3	152.26	17917	0.007637
		4	155.36	23164	0.007896
		5	158.06	22246	0.007234
	1.10	1	146.66	27484	0.009533
		2	154.79	25291	0.019219
		3	104.28	29255	0.006409
		4	139.27	17232	0.025738
		5	151.27	22941	0.009786
	1.20	1	172.96	20883	0.010674
		2	144.57	21452	0.006831
		3	196.88	21256	0.010521
		4	194.18	20963	0.010084
		5	142.46	20961	0.006919

Table A 2: Flexural test results

Nozzle Diameter (mm)	Spacing (mm)	Sample Number	Flexural Strength (MPa)	Flexural Modulus (MPa)	Ultimate Flexural Strain (mm/mm)
0.80	0.75	1	347.04	16502	0.024699
		2	373.58	18272	0.024706
		3	375.38	16734	0.025923
		4	399.72	18259	0.026008
	0.80	1	310.73	14685	0.024096
		2	343.24	14836	0.025873
		3	289.71	13600	0.022542
		4	196.93	8371	0.025097
		5	344.94	16893	0.021894
1.00	0.85	1	291.76	133346	0.023167
		2	326.25	16376	0.020776
		3	312.67	15443	0.021339
		4	294.25	13397	0.023072
		5	305.45	14533	0.021829
	0.92	1	354.99	16426	0.022547
		2	284.89	12169	0.025846
		3	292.93	12028	0.027154
		4	259.74	11201	0.025314
		5	338.25	14988	0.024409
	1.00	1	276.09	11003	0.027874
		2	275.06	11538	0.026521
		3	243.22	8675	0.030581
		4	291.34	11547	0.027232
		5	325.57	14382	0.024352
1.2	1.00	1	252.49	11316	0.023274
		2	263.43	11054	0.026324
		3	310.36	13783	0.024057
		4	281.47	11764	0.025798
		5	312.60	13367	0.024153
	1.10	1	238.47	12348	0.019758
		2	260.97	11753	0.023813
		3	193.70	9339	0.021187
		4	229.32	11183	0.21566
		5	259.55	11477	0.023881
	1.20	1	229.13	10232	0.024432
		2	227.74	9940	0.0247
		3	180.21	7415	0.025357
		4	200.47	9224	0.023074
		5	266.79	12314	0.023233

APPENDIX B. BURNOFF TEST RESULTS

Table B 1: Burnoff test results

Nozzle Diameter (mm)	Spacing (mm)	Sample Number	Fiber Volume Fraction (%)
0.80	0.75	1	17.30
		2	17.61
		3	18.57
		4	18.23
		5	18.79
	0.80	1	17.87
		2	17.81
		3	18.23
		4	18.51
		5	18.64
1.00	0.85	1	16.95
		2	17.40
		3	17.66
		4	17.33
		5	17.20
	0.92	1	16.88
		2	17.25
		3	17.19
		4	16.81
		5	17.30
	1.00	1	16.96
		2	16.96
		3	16.87
		4	17.03
		5	17.14
1.2	1.00	1	15.49
		2	15.97
		3	16.27
		4	15.01
		5	15.62
	1.10	1	14.32
		2	14.80
		3	14.92
		4	15.38
		5	15.57
	1.20	1	14.11
		2	14.03
		3	14.06
		4	14.44
		5	14.70

APPENDIX C. SURFACE ROUGHNESS RESULTS

Table C 1: Surface roughness values (Sa) for prints with 1.2 mm nozzle

		Resin Flow Rate (cc/hr)							
		4.81	4.50	4.29	3.91	3.62	3.37	3.05	2.75
Spacing (mm)	1.25	41	45	79	98	82	96	108	109
	1.2	43	45	74	70	89	104	145	108
	1.15	44	59	77	45	88	99	122	83
	1.1	37	49	56	76	86	92	112	116
	1.05	42	41	58	65	98	80	90	88
	1.00	42	45	55	69	107	105	112	91
	0.95	38	59	53	53	74	108	105	72
	0.90	38	38	46	36	91	78	89	89

Sa values are in mm.

Table C 2:Surface roughness values (Sa) for prints with 1.0 mm nozzle

		Resin Flow Rate (cc/hr)						
		4.50	4.29	3.91	3.62	3.37	3.05	2.75
Spacing (mm)	1.07	64	59	45	63	75	78	88
	1.00	48	57	37	41	49	67	65
	0.92	30	57	35	37	44	67	65
	0.85	43	66	35	57	48	49	64
	0.78	45	43	33	48	63	61	55

Sa values are in mm.

Table C 3: Surface roughness values (Sa) for prints with 0.8 mm nozzle.

		Resin Flow Rate (cc/hr)					
		3.62	3.37	3.05	2.75	2.43	2.11
Spacing (mm)	0.80	84	37	67	49	38	47
	0.75	68	45	68	61	40	57

APPENDIX D. ARDUINO CODE (PRINTER MOTION)

```
/*
 * Length 23000 ; Z 640
 * for nozzle .8mm and spacing=.8mm y=58
for nozzle 1mm and spacing=1mm y=72
for 1.2 mm nozzle and 1.2 mm spacing y=86
For profile check y=250
for 1.2 mm nozzle, 1.0 mm spacing y=72
For 1.2mm nozzle, 1.1 mm spacing y=79
for 1.0 mm n0zzle, 0.85 spacing y=62
for 1.0 mm nozzle 0.92mm spacing y=67
corner delay =2000 for 1.2 mm nozzle and 1.2 mm spacing and resin delay 09
corner delay = 1000 for 1.2 mm nozzle, 1.0 mm spacing,
corner delay = 2000 for 1.2 mm nozzle, 1.0 mm spacing,
corner delay = 2000 for 1.2 mm nozzle, 1.1 mm spacing,
corner delay = 2000 for 1.0 mm nozzle, 0.85 mm spacing,
For DMA
length = 25000 or, 26000
1.2 mm nozzle rster number 6
1.0 mm nozzle raster number 6
0.8 mm nozzle raster number 7*/
#define distance_x 25000
#define distance_y 72
#define distance_z 640
#define z_adjustment_long 30000
#define z_adjustment_fine 50
#define decrease_x 10
#define start_button 31
#define stop_button 27
#define pause_button 29
#define z_up_fine 30
#define z_down_fine 25
#define z_up_long 26
#define z_down_long 28
#define x_motor_step 13
#define x_motor_direction 12
#define y_motor_step 11
#define y_motor_direction 10
#define z_motor_step 9
#define z_motor_direction 8
int length_x;
int start = false;
int setting = false;
int raster = 8;
```

```
int layer = 6;
int odd;
int dl1 = 1000;          /*speed control here*/
int corner_delay = 1000; /*controlls excess resin at the corner*/
int adjust_delay = 100;
int wait_after_adjustment = 500;
int z_delay = 100;
int line_num_x = raster * 2;
int line_num_y = line_num_x - 1;
int curr_line_num_x = 1;
int curr_line_num_y = 1;
int curr_layer = 1;
int direction_x;
int direction_y;
int direction_z;
int pos_x = 0;
int pos_y = 0;
int pos_z = 0;
int pause_tag = 1;
void setup() {
  pinMode(stop_button, INPUT);        /* stop button*/
  pinMode(start_button, INPUT);       /* Start button*/
  pinMode(x_motor_step, OUTPUT);      /* x motor step*/
  pinMode(x_motor_direction, OUTPUT); /* x motor direction*/
  pinMode(y_motor_step, OUTPUT);      /* y motor step*/
  pinMode(y_motor_direction, OUTPUT); /* y motor direction*/
  pinMode(z_motor_step, OUTPUT);      /* z motor step*/
  pinMode(z_motor_direction, OUTPUT); /* z motor direction*/
  pinMode(pause_button, INPUT);       /* Pause button*/
  pinMode(z_down_fine, INPUT);        /* Z fine down button*/
  pinMode(z_up_fine, INPUT);          /* Z fine Up button*/
  pinMode(z_down_long, INPUT);        /* Z long down button*/
  pinMode(z_up_long, INPUT);          /* Z long up button*/
  digitalWrite(x_motor_step, LOW);
  digitalWrite(y_motor_step, LOW);
  digitalWrite(z_motor_step, LOW);
  digitalWrite(x_motor_direction, LOW);
  digitalWrite(y_motor_direction, LOW);
  digitalWrite(z_motor_direction, LOW);
  Serial.begin(57600);
  pinMode(44, OUTPUT);
  pinMode(46, OUTPUT);
  pinMode(48, OUTPUT);
  pinMode(50, OUTPUT);
  Serial.begin(115200);
```

```
}
void loop() {
  /*Initiates process by pressing start button*/
  if (digitalRead(start_button) == LOW && digitalRead(stop_button) == HIGH)
    start = true;
  /*Will enter the print if current layer number is less than max layer number,
    Also checks the START status*/
  if (curr_layer <= layer && start == true) {
    /*Set direction of line x*/
    if (curr_line_num_x % 2 == 1) direction_x = 1;
    else direction_x = 2;
    /*Set direction of line y*/
    if (curr_layer % 2 == 1) direction_y = 1;
    else direction_y = 2;
    /*Set direction of line x*/
    direction_z = 1;
    /*starting loop for X line
      Goes into the if block if pause tag=1*/
    if (curr_line_num_x <= line_num_x && pause_tag == 1) {
      length_x = (distance_x - (curr_layer - 1) * (decrease_x * 2));
      for (int x = pos_x; x <= length_x && start == true; x++) {
        Serial.print(x, '\n');
        /*one step of x for next block of code*/
        if (direction_x == 1) {
          digitalWrite(x_motor_direction, LOW);
          digitalWrite(48, HIGH);
          digitalWrite(50, HIGH);
          digitalWrite(44, LOW);
          digitalWrite(46, LOW);
        } else {
          digitalWrite(x_motor_direction, HIGH);
          digitalWrite(44, HIGH);
          digitalWrite(46, HIGH);
          digitalWrite(48, LOW);
          digitalWrite(50, LOW);
        }
        digitalWrite(x_motor_step, HIGH);
        delayMicroseconds(dl1);
        digitalWrite(x_motor_step, LOW);
        delayMicroseconds(dl1); /*one step done here*/
        /*delay for excess resin at the end the turn*/
        if (x == (length_x - (1))) {
          delay(corner_delay);
        }
        /*checks wheather pause button is pressed*/
```

```
        if (digitalRead(pause_button) == LOW) {
          start = false;
          pos_x = x;
          pause_tag = 1;
          digitalWrite(44, LOW);
          digitalWrite(46, LOW);
          digitalWrite(48, LOW);
          digitalWrite(50, LOW);
        }
        /*checks whether STOP button is pressed*/
        if (digitalRead(stop_button) == LOW) {
          start = false;
          curr_line_num_x = 1;
          curr_line_num_y = 1;
          curr_layer = 1;
          pos_x = 0;
          pos_y = 0;
          pause_tag = 1;
          digitalWrite(44, LOW);
          digitalWrite(46, LOW);
          digitalWrite(48, LOW);
          digitalWrite(50, LOW);
        }
      } /*one line of x is done here*/
      if (start == true) {
        pos_x = 0; /*when one x line is completed, resets resets position of x to
zero.  As X line is complete pause tag is set to 2 */
        pause_tag = 2;
      }
      digitalWrite(x_motor_direction, LOW); /*Actually does nothing*/
      if (start == true) curr_line_num_x++; /*updating x line number*/
    }                                       /*finishing loop of X line*/
    /*starting loop for Y line
      Goes into the if block if pause tag=2    */
    if (curr_line_num_y <= line_num_y && pause_tag == 2) {
      for (int y = pos_y; y <= distance_y && start == true; y++) {
        if (direction_y == 1) digitalWrite(y_motor_direction, HIGH);
        else digitalWrite(y_motor_direction, LOW);
        digitalWrite(y_motor_step, HIGH);
        delayMicroseconds(dl1);
        digitalWrite(y_motor_step, LOW);
        delayMicroseconds(dl1);

        if (digitalRead(pause_button) == LOW) {
          start = false;
```

```
          pos_y = y;
          pause_tag = 2;
        }
        if (digitalRead(stop_button) == LOW) {
          start = false;
          curr_line_num_x = 1;
          curr_line_num_y = 1;
          curr_layer = 1;
          pos_x = 0;
          pos_y = 0;
          pause_tag = 1;
        }
      }
      if (start == true) {
        pos_y = 0; /*when one Y line is completed, resets resets position of Y to
zero.  As Y line is complete pause tag is set to 1 */
        pause_tag = 1;
      }
      digitalWrite(y_motor_direction, LOW);
      if (start == true) curr_line_num_y++;
    }
    if (curr_layer <= layer && curr_line_num_x > line_num_x) {
      for (int z = 0; z <= distance_z && start == true; z++) {
        digitalWrite(z_motor_direction, LOW);
        digitalWrite(z_motor_step, HIGH);
        delayMicroseconds(z_delay);
        digitalWrite(z_motor_step, LOW);
        delayMicroseconds(z_delay);
      }
      digitalWrite(z_motor_direction, LOW);
      curr_line_num_x = 1;
      curr_line_num_y = 1; /*sets line numbers of x and y to initial conditions*/
      curr_layer++;
      pause_tag = 1;
      for (int x = 0; x <= decrease_x && start == true; x++) {
        direction_x = 1;
        if (direction_x == 1) digitalWrite(x_motor_direction, LOW);
        else digitalWrite(x_motor_direction, HIGH);
        digitalWrite(48, LOW);
        digitalWrite(50, LOW);
        digitalWrite(44, LOW);
        digitalWrite(46, LOW);
        digitalWrite(x_motor_step, HIGH);
        delayMicroseconds(dl1);
        digitalWrite(x_motor_step, LOW);
```

```
      delayMicroseconds(dl1); /*one step done here*/
    }
  }
}
if (curr_layer > layer) {
  start = false;
  curr_line_num_x = 1;
  curr_line_num_y = 1;
  curr_layer = 1;
  pos_x = 0;
  pos_y = 0;
  pause_tag = 1;
}
/*Z adjustment here*/
setting = false;
if (start == false) {
  if (start == false && digitalRead(z_down_fine) == LOW) {
    setting = true;
    for (int zfd = 0; setting == true && zfd < z_adjustment_fine; zfd++) {
      digitalWrite(z_motor_direction, HIGH);
      digitalWrite(z_motor_step, HIGH);
      delayMicroseconds(adjust_delay);
      digitalWrite(z_motor_step, LOW);
      delayMicroseconds(adjust_delay);
      if (digitalRead(stop_button) == LOW) setting = false;
    }
    delay(wait_after_adjustment);
  }
  if (start == false && digitalRead(z_up_fine) == LOW) {
    setting = true;
    for (int zfu = 0; setting == true && zfu < z_adjustment_fine; zfu++) {
      digitalWrite(z_motor_direction, LOW);
      digitalWrite(z_motor_step, HIGH);
      delayMicroseconds(adjust_delay);
      digitalWrite(z_motor_step, LOW);
      delayMicroseconds(adjust_delay);
      if (digitalRead(stop_button) == LOW) setting = false;
    }
    delay(wait_after_adjustment);
  }
  if (start == false && digitalRead(z_down_long) == LOW) {
    setting = true;
    for (int zld = 0; setting == true && zld < z_adjustment_long; zld++) {
      digitalWrite(z_motor_direction, HIGH);
      digitalWrite(z_motor_step, HIGH);
```

```
        delayMicroseconds(adjust_delay);
        digitalWrite(z_motor_step, LOW);
        delayMicroseconds(adjust_delay);
        if (digitalRead(stop_button) == LOW) setting = false;
      }
      delay(wait_after_adjustment);
    }
    if (start == false && digitalRead(z_up_long) == LOW) {
      setting = true;
      for (int zlu = 0; setting == true && zlu < z_adjustment_long; zlu++) {
        digitalWrite(z_motor_direction, LOW);
        digitalWrite(z_motor_step, HIGH);
        delayMicroseconds(adjust_delay);
        digitalWrite(z_motor_step, LOW);
        delayMicroseconds(adjust_delay);
        if (digitalRead(stop_button) == LOW) setting = false;
      }
      delay(wait_after_adjustment);
    }
  }
}
```

APPENDIX E. ARDUINO CODE (RESIN DRIVE)

```
/*nozzle .8mm slowDelay=14
nozzle 1mm slowDelay=12
nozzle 1.2mm, slowDelay=9
nozzle 1.2mm, spacing 1.0, slow delay 11
nozzle 1.2 spacing 1.1, slowDelay 10
nozzle 1.0 spacing 0.85 slowDelay 13
nozzle 1.0 spacing 0.92 slowDelay 12 */
#define walkDown 12
#define walkUp 11
#define stopAll 10
#define runDown 9
#define runUp 8
#define motorDirection 3
#define motorStep 4
#define slowDelay 6.8
int go = 0;
bool goDown = false;
bool goUp = false;
void setup() {
  pinMode(walkDown, INPUT);
  pinMode(walkUp, INPUT);
  pinMode(runDown, INPUT);
  pinMode(runUp, INPUT);
  pinMode(stopAll, INPUT);
  pinMode(motorStep, OUTPUT);
  pinMode(motorDirection, OUTPUT);
}
void loop() {
  if (digitalRead(runDown) == LOW) {
    digitalWrite(motorDirection, HIGH);
    digitalWrite(motorStep, HIGH);
    delay(0.001);
    digitalWrite(motorStep, LOW);
    delay(0.001);
  }
  if (digitalRead(runUp) == LOW) {
    digitalWrite(motorDirection, LOW);
    digitalWrite(motorStep, HIGH);
    delay(0.001);
    digitalWrite(motorStep, LOW);
    delay(0.001);
  }
  if (digitalRead(walkDown) == LOW && digitalRead(stopAll) == HIGH) {
```

```
    goDown = true;
    while (goDown) {
      digitalWrite(motorDirection, HIGH);
      digitalWrite(motorStep, HIGH);
      delay(slowDelay);
      digitalWrite(motorStep, LOW);
      delay(slowDelay);
      if (digitalRead(stopAll) == LOW) { goDown = false; }
    }
  }
  if (digitalRead(walkUp) == LOW && digitalRead(stopAll) == HIGH) {
    goUp = true;
    while (goUp) {
      digitalWrite(motorDirection, LOW);
      digitalWrite(motorStep, HIGH);
      delay(slowDelay);
      digitalWrite(motorStep, LOW);
      delay(slowDelay);
      if (digitalRead(stopAll) == LOW) { goUp = false; }
    }
  }
}
```